Signal to Noise Ratio Analysis in Virtual Source Array Imaging[*]

Josselin Garnier[†], George Papanicolaou[‡], Adrien Semin[§], and Chrysoula Tsogka[¶]

Abstract. We consider correlation-based imaging of a reflector located on one side of a passive array where the medium is homogeneous. On the other side of the array the illumination by remote impulsive sources goes through a strongly scattering medium. It has been shown in [J. Garnier and G. Papanicolaou, *Inverse Problems*, 28 (2012), 075002] that migrating the cross correlations of the passive array gives an image whose resolution is as good as if the array was active and the array response matrix was that of a homogeneous medium. In this paper we study the signal to noise ratio (SNR) of the image as a function of statistical properties of the strongly scattering medium, the signal bandwidth, and the source and passive receiver array characteristics. Using a Kronecker model for the strongly scattering medium we show that image resolution is as expected and that the SNR can be computed in an essentially explicit way. We show with direct numerical simulations using full wave propagation solvers in random media that the theoretical predictions based on the Kronecker model are accurate.

Key words. imaging, wave propagation, random media, cross correlation, Kronecker model

AMS subject classifications. 35R60, 86A15

DOI. 10.1137/140968677

1. Introduction. Images of reflectors obtained with sensor arrays have resolution that depends on the size of the array, the central wavelength and bandwidth of the probing signal, and the distance of the reflector from the array (the range). The resolution improves as the size of the array increases and is best when it encloses the reflector. It also improves as the bandwidth increases. This is because the duration of the probing pulses sent by the array is proportional to the inverse of the bandwidth and the identification of the received echoes is more accurate for narrow pulses. However, image resolution deteriorates rapidly when the medium between the reflector to be imaged and the sensor array is inhomogeneous, and multiple scattering generates recorded signals (traces), in which the echoes from the reflector to be imaged are obscured.

In this paper we consider the situation in which it is possible to have a passive, auxiliary array, as shown in Figure 1, that is closer to the reflector to be imaged. This situation was first considered in exploration geophysics [1, 25, 27] and it was studied mathematically in [18, 19].

[†]Laboratoire de Probabilités et Modèles Aléatoires & Laboratoire Jacques-Louis Lions, Université Paris VII, 75205 Paris Cedex 13, France (garnier@math.univ-paris-diderot.fr). The research of this author was partially supported by ERC Advanced grant Project MULTIMOD-26718.

[‡]Mathematics Department, Stanford University, Stanford, CA 94305 (papanicolaou@stanford.edu). The research of this author was partially supported by AFOSR grant FA9550-11-1-0266.

[§]Institut für Mathematik, Technical University of Berlin, 10587 Berlin, Germany (semin@math.tu-berlin.de).

[¶]Applied Mathematics, University of Crete, GR-70013 Heraklion, Greece, and IACM/FORTH, GR-71409 Heraklion, Greece (tsogka@tem.uoc.gr).

In hydrocarbon reservoir exploration and monitoring, the seismic sources and receivers are located on the surface, over a region of interest several kilometers below. However, the top layers of the earth's crust are strongly scattering, the so-called overburden, and therefore the images are noisy and often hard to interpret. If it is possible to deploy auxiliary, passive receiver arrays below ground, in boreholes, for example, then the recorded signals on these arrays can be used to image with improved clarity the region further below.

Since the traces recorded at an auxiliary passive array appear to be asynchronously generated, with the illumination from the surface having passed through the scattering medium, it is necessary to image by migrating, or back-propagating, the cross correlations of the traces. In fact, the use of cross correlations virtually eliminates the effects of multiple scattering when the imaging setup is as in Figure 1. As noted in [18, 19], this is because using a time reversal interpretation of the cross correlations allows us to identify the matrix formed by them as the array response matrix of the auxiliary array as if it were in active rather than passive mode. This is why this type of imaging with cross correlations is also called virtual source imaging. We may motivate imaging by migrating the cross correlations by analogy with ambient noise imaging [15, 16, 17, 27] if we think of wave propagation through the randomly scattering medium as producing signals that appear to come from spatially uncorrelated noise sources. If the noise sources surround the auxiliary array and the reflector to be imaged, then the Kirchhoff–Helmholtz identity can be used [16, 27], which shows that the integral of the cross correlation of signals from different sensors of the auxiliary array is essentially equal to the symmetrized Green's function between these sensors, and hence includes travel time information from the reflector to be imaged. This is the essential information needed in migration imaging. If the support of the noise sources is spatially limited, then the diversity of the illumination coming from them will likely be enhanced by passing through the scattering medium, and it will appear to have originated from a wider source distribution than the one that generated it. This can be shown to be the case analytically for isotropic random media [19].

The purpose of this paper is to analyze the signal to noise ratio (SNR) of the image from auxiliary passive array data using a Kronecker model for the effects of multiple scattering, which is a simple but effective phenomenological model that works well in virtual source imaging. This is shown by comparing the theoretical results with those obtained with fully resolved direct numerical simulations of wave propagation in strongly scattering media for both resolution and the SNR. We also compare the resolution analysis with the asymptotic theory in the random paraxial regime. The Kronecker model and the representation of the array data are presented in section 3. The mean of the image is calculated in section 4 and the SNR in section 6, which contains the main theoretical results of the paper in Proposition 6.2. It is shown that the SNR of the image improves with the density of the auxiliary passive array and on the array of sources but only up to a critical intersensor distance, which is determined by the scattering properties of the medium. The numerical simulations are presented in section 7 and they support the theory very well.

2. Formulation of the imaging problem. To describe more precisely the imaging problem, we give a brief mathematical formulation. The space coordinates are denoted by $\vec{\boldsymbol{x}} = (\boldsymbol{x}, z) \in \mathbb{R}^2 \times \mathbb{R}$. The waves are emitted by a point source located at $\vec{\boldsymbol{x}}_s$ which belongs to an array of

sources $(\vec{x}_s)_{s=1,\ldots,N_s}$ located at the surface, in the plane $z = 0$. Throughout the paper we use the subscript s (as well as s') in $\vec{x}_s$ to indicate source location. The waves are recorded by an auxiliary passive array of receivers $(\vec{x}_q)_{q=1,\ldots,N_q}$ located in the plane $z = -L$ (see Figure 1). We use the subscript q (as well as q') in $\vec{x}_q$ to denote receiver location on the auxiliary array. The recorded signals form the data matrix

$$(2.1) \qquad \left\{ u(t, \vec{x}_q; \vec{x}_s), \, t \in \mathbb{R}, \, q = 1, \ldots, N_q, \, s = 1, \ldots, N_s \right\}.$$

The waves can also be recorded at the illuminating, active array as well, so as to compare the quality of images obtained when an auxiliary passive array is not available. We denote the data matrix in this case by $\left\{ u(t, \vec{x}_r; \vec{x}_s), \, t \in \mathbb{R}, \, r = 1, \ldots, N_r, \, s = 1, \ldots, N_s \right\}$, with the difference being that $\vec{x}_r$ denotes the location of a receiver on the surface array (in the plane $z = 0$) while $\vec{x}_q$ denotes that of a receiver on the auxiliary passive array (in the plane $z = -L$). We use the subscript r (as well as r') in $\vec{x}_r$ to denote receiver location on the primary array in the plane $z = 0$.

The wave field $(t, \vec{x}) \mapsto u(t, \vec{x}; \vec{x}_s)$ satisfies the scalar wave equation

$$(2.2) \qquad \frac{1}{c(\vec{x})^2} \frac{\partial^2 u}{\partial t^2} - \Delta u = \nabla \cdot \vec{F}(t, \vec{x}; \vec{x}_s),$$

where $c(\vec{x})$ is the speed of propagation in the medium and the forcing term $(t, \vec{x}) \mapsto \vec{F}(t, \vec{x}; \vec{x}_s)$ models the source. We take the source to be point-like, located at $\vec{x}_s = (\boldsymbol{x}_s, 0)$, and emitting a pulse $F(t)$ with carrier frequency ω_0 and bandwidth B:

$$(2.3) \qquad \vec{F}(t, \vec{x}; \vec{x}_s) = \vec{e}_z F(t) \delta(z) \delta(\boldsymbol{x} - \boldsymbol{x}_s).$$

We consider a randomly scattering medium that occupies the section $z \in (-L, 0)$ and is sandwiched in between two homogeneous half-spaces:

$$(2.4) \qquad \frac{1}{c(\vec{x})^2} = \frac{1}{c_0^2} \left(1 + \mu(\vec{x}) \right), \qquad \vec{x} \in \mathbb{R}^2 \times (-L, 0).$$

Here $\mu(\vec{x})$ is a zero-mean stationary random process modeling the random heterogeneities present in the medium.

The homogeneous half-space $z < -L$ is matched to the random section $z \in (-L, 0)$. We want to image a reflector below the random medium, placed at $\vec{y} = (\boldsymbol{y}, -L_y)$, $L_y > L$. The reflector is modeled by a local change of the speed of propagation of the form

$$\frac{1}{c(\vec{x})^2} = \frac{1}{c_0^2} \left(1 + \frac{\sigma_{\text{ref}}}{|\Omega_{\text{ref}}|} \mathbf{1}_{\Omega_{\text{ref}}}(\vec{x} - \vec{y}) \right), \qquad \vec{x} \in \mathbb{R}^2 \times (-\infty, -L),$$

where Ω_{ref} is a small domain and σ_{ref} is the reflectivity of the reflector.

The goal is to image the location of the reflector from the data set (2.1). We will study the imaging function introduced in [18] that migrates the cross correlation of the recorded signals:

$$(2.5) \qquad \mathcal{I}_{\text{CC}}(\vec{y}^S) = \sum_{q,q'=1}^{N_q} \mathcal{C}\left(\mathcal{T}(\vec{x}_q, \vec{y}^S) + \mathcal{T}(\vec{y}^S, \vec{x}_{q'}), \vec{x}_q, \vec{x}_{q'} \right),$$
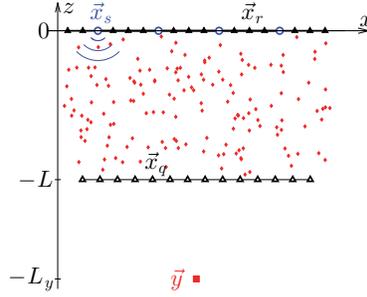
Figure 1. *Sensor array imaging of a reflector through a scattering medium in the region $z \in (-L, 0)$. $\vec{\boldsymbol{x}}_s$ is a source, $\vec{\boldsymbol{x}}_r$ is a receiver in the surface array, $\vec{\boldsymbol{x}}_q$ is a receiver in the auxiliary array, and $\vec{\boldsymbol{y}}$ is the reflector.*

where $\mathcal{T}(\vec{\boldsymbol{x}}, \vec{\boldsymbol{y}}) = |\vec{\boldsymbol{x}} - \vec{\boldsymbol{y}}|/c_0$ is the travel time from $\vec{\boldsymbol{y}}$ to $\vec{\boldsymbol{x}}$ in a homogeneous medium with speed of propagation c_0 and

$$(2.6) \qquad \mathcal{C}\big(\tau, \vec{\boldsymbol{x}}_q, \vec{\boldsymbol{x}}_{q'}\big) = \sum_{s=1}^{N_s} \int_{\mathbb{R}} u\big(t, \vec{\boldsymbol{x}}_q; \vec{\boldsymbol{x}}_s\big) u\big(t + \tau, \vec{\boldsymbol{x}}_{q'}; \vec{\boldsymbol{x}}_s\big) dt.$$

We refer to the argument $\vec{\boldsymbol{y}}^S$ as the search point in the image domain and we expect the imaging function to have a peak when $\vec{\boldsymbol{y}}^S$ is at or near the true reflector location $\vec{\boldsymbol{y}}$.

The usual travel time migration imaging with the active array is done with the Kirchhoff migration imaging function [2, 3]

$$\mathcal{I}_{\mathrm{KM}}(\vec{\boldsymbol{y}}^S) = \sum_{s=1}^{N_s} \sum_{r=1}^{N_r} u\big(\mathcal{T}(\vec{\boldsymbol{x}}_r, \vec{\boldsymbol{y}}^S) + \mathcal{T}(\vec{\boldsymbol{y}}^S, \vec{\boldsymbol{x}}_s), \vec{\boldsymbol{x}}_r; \vec{\boldsymbol{x}}_s\big),$$

which for strongly scattering media gives a bad image, as is clearly seen in our numerical simulations in section 7.

3. Representation and statistical description of the recorded field. We address the finite source aperture case, in which the sources do not cover the whole surface $z = 0$. We now state the two main hypotheses under which the results in this paper hold. The first hypothesis deals with the statistics of the field in the random medium. The second hypothesis deals with scattering from the reflector to be imaged. The Fourier transform is defined here as

$$\hat{F}(\omega) = \int F(t) e^{i\omega t} dt.$$

3.1. The Kronecker model for propagation in a strongly scattering medium. We assume that the medium is strongly scattering so that the complex field that is transmitted through the random medium has Gaussian statistics, mean zero, and cross correlations of the form

$$(3.1) \qquad \mathbb{E}\big[\hat{u}_0(\omega, \vec{\boldsymbol{x}}_q; \vec{\boldsymbol{x}}_s) \hat{u}_0(\omega', \vec{\boldsymbol{x}}_{q'}; \vec{\boldsymbol{x}}_{s'})\big] = 0,$$

and

$$\mathbb{E}\big[\hat{u}_0(\omega, \vec{\boldsymbol{x}}_q; \vec{\boldsymbol{x}}_s)\overline{\hat{u}_0(\omega', \vec{\boldsymbol{x}}_{q'}; \vec{\boldsymbol{x}}_{s'})}\big] = \hat{F}(\omega)\overline{\hat{F}(\omega')} \exp\Big(-\frac{(\omega - \omega')^2}{\omega_{\mathrm{c}}^2}\Big)$$

(3.2)
$$\times \exp\Big(-\frac{|\boldsymbol{x}_q - \boldsymbol{x}_{q'}|^2}{X_{\mathrm{cq}}^2} - \frac{|\boldsymbol{x}_s - \boldsymbol{x}_{s'}|^2}{X_{\mathrm{cs}}^2}\Big)$$

for ω, ω' in the bandwidth $[\omega_0 - B/2, \omega_0 + B/2]$ of the source, for $\vec{\boldsymbol{x}}_s, \vec{\boldsymbol{x}}_{s'} \in [-b/2, b/2]^2 \times \{0\}$ in the source array, and for $\vec{\boldsymbol{x}}_q, \vec{\boldsymbol{x}}_{q'} \in [-a/2, a/2]^2 \times \{-L\}$ in the auxiliary receiver array. We also have $\hat{u}_0(-\omega, \vec{\boldsymbol{x}}_q; \vec{\boldsymbol{x}}_s) = \overline{\hat{u}_0(\omega, \vec{\boldsymbol{x}}_q; \vec{\boldsymbol{x}}_s)}$ for any ω in the bandwidth $[\omega_0 - B/2, \omega_0 + B/2]$ of the source, since the time-dependent wave field is a real-valued quantity. We refer to (3.2) as the wave field covariance.

There should be a multiplicative constant in formula (3.2), but we take it equal to one as it does not play any role in the following. The parameter ω_{c} is the correlation frequency of the incoherent field in the plane $z = -L$ of the auxiliary receiver array, X_{cq} is the correlation radius of the field at the auxiliary receiver array (when emitted from a point source at the source array), and X_{cs} is the correlation radius of the field at the source array (when emitted from a point source at the auxiliary receiver array). Since the complex field is assumed to have Gaussian statistics, these three parameters fully characterize the statistical properties of the illumination of the region below the auxiliary receiver array, where the reflector to be imaged is located.

The separable form (3.2) of the field covariance function (separable in functions of the frequency offsets $\omega - \omega'$, the source offsets $\boldsymbol{x}_s - \boldsymbol{x}_{s'}$, and the receiver offsets $\boldsymbol{x}_q - \boldsymbol{x}_{q'}$) is a model that has been proposed and used in the wireless telecommunication literature, in order to analyze the behavior of telecommunication systems in strongly scattering and statistically homogeneous random media. It is called the Kronecker model [9]. The Gaussian form of the covariance function (in frequency offsets and position offsets) allows us to get simple closed-form formulas, but this hypothesis can be relaxed.

The assumption of Gaussian statistics for the field is the key one needed for the SNR analysis but is not used in the resolution analysis of the imaging function. It can be relaxed in the sense that we only need a sub-Gaussianity assumption, that is, that the fourth-order moments can be bounded from above by those of a Gaussian process of the same covariance. It is widely accepted that in strongly scattering media the statistics of the wave fields (for at least the lower moments) have Gaussian-like behavior, resulting in an exponential distribution for the intensity [14, 24, 26]. This is consistent with experiments of laser beam propagation through a turbulent atmosphere, where saturation of intensity fluctuations is observed, and with the scintillation index approaching unity [22]. The fourth-order moment properties of the wave fields coming from the Gaussian assumption are also used frequently in wireless telecommunications [9, 11, 23] associated with Rayleigh fading channels.

It is not within the scope of this paper to relate the proposed model for the complex field that is transmitted through the random medium in $[-L, 0]$ to a particular asymptotic regime for wave propagation in random media. Rather, we use this model as a benchmark to derive the SNR results that direct numerical simulations clearly support. As far as resolution is concerned, usually only second-order moments are needed, and several theories derived

from first principles are consistent with second moments of the form (3.2). We review this in section 5 where we show how the correlation length X_{cq} is related to the statistics of the random medium in the paraxial regime. We refer the reader to [19] where the random paraxial regime and another—that of randomly layered media—are considered in detail in the same context of virtual source imaging. The field covariance function in a general, interferometric imaging context was also studied in the random paraxial regime in [5, Appendix B] and in the random travel time model in [4]. In [4] SNR calculations of the image are also carried out using fourth moments, which are computable for the random travel time model. However, the random travel time model is appropriate only for weakly scattering media, and the wave field statistics are not Gaussian, a regime that is very different from the one where the Kronecker model is applicable.

3.2. Born approximation for the field scattered by the reflector. We consider only the Born approximation for the point-like reflector, as in [21, 18, 19], so that the field recorded at the receiver $\vec{x}_q$ is given by

(3.3)
$$
\begin{aligned}
\hat{u}(\omega, \vec{x}_q; \vec{x}_s) &= \hat{u}_0(\omega, \vec{x}_q; \vec{x}_s) \\
&\quad - 2i\frac{\omega^3 \sigma_{\mathrm{ref}}}{c_0^3} \int_{\mathbb{R}^2} \hat{G}_0(\omega, \vec{x}_q; \vec{y}) \hat{G}_0(\omega, \vec{y}; (\boldsymbol{x}, -L)) \hat{u}_0(\omega, (\boldsymbol{x}, -L); \vec{x}_s) d\boldsymbol{x},
\end{aligned}
$$

where $\hat{u}_0(\omega, \vec{z}; \vec{x}_s)$ is the field transmitted through the random medium that illuminates the point $\vec{z}$ and $\hat{G}_0(\omega, \vec{x}; \vec{y})$ is the homogeneous three-dimensional Green's function

(3.4)
$$
\hat{G}_0(\omega, \vec{x}; \vec{y}) = \frac{1}{4\pi|\vec{x} - \vec{y}|} \exp\left(i\frac{\omega}{c_0}|\vec{x} - \vec{y}|\right).
$$

This Green's function is used in (3.3) since the medium is assumed homogeneous in the region $z \in [-L_y, -L]$ between the auxiliary receiver array and the reflector.

The expression (3.3) can be obtained from the following arguments. First, the classical Born approximation for the reflector [8, section 13.1.2] gives that

$$
\begin{aligned}
\hat{u}(\omega, \vec{x}_q; \vec{x}_s) &= \hat{u}_0(\omega, \vec{x}_q; \vec{x}_s) + \omega^2 \int_{\mathbb{R}^3} \hat{G}_0(\omega, \vec{x}_q; \vec{z}) \left(\frac{1}{c^2(\vec{z})} - \frac{1}{c_0^2}\right) \hat{u}_0(\omega, \vec{z}; \vec{x}_s) d\vec{z} \\
&= \hat{u}_0(\omega, \vec{x}_q; \vec{x}_s) + \frac{\omega^2 \sigma_{\mathrm{ref}}}{c_0^2 |\Omega_{\mathrm{ref}}|} \int_{\Omega_{\mathrm{ref}}} \hat{G}_0(\omega, \vec{x}_q; \vec{y} + \vec{z}) \hat{u}_0(\omega, \vec{y} + \vec{z}; \vec{x}_s) d\vec{z}.
\end{aligned}
$$

If the reflector is small, the point approximation gives [18]

(3.5)
$$
\hat{u}(\omega, \vec{x}_q; \vec{x}_s) = \hat{u}_0(\omega, \vec{x}_q; \vec{x}_s) + \frac{\omega^2 \sigma_{\mathrm{ref}}}{c_0^2} \hat{G}_0(\omega, \vec{x}_q; \vec{y}) \hat{u}_0(\omega, \vec{y}; \vec{x}_s),
$$

where $\hat{u}_0(\omega, \vec{y}; \vec{x}_s)$ is the field that illuminates the reflector. From the Green's theorem, we have

$$
\begin{aligned}
\hat{u}_0(\omega, \vec{y}; \vec{x}_s) = \int_{\mathbb{R}^2} &\partial_z \hat{u}_0(\omega, (\boldsymbol{x}, -L); \vec{x}_s) \hat{G}_0(\omega, (\boldsymbol{x}, -L); \vec{y}) \\
&- \hat{u}_0(\omega, (\boldsymbol{x}, -L); \vec{x}_s) \partial_z \hat{G}_0(\omega, (\boldsymbol{x}, -L); \vec{y}) d\boldsymbol{x},
\end{aligned}
$$

which, when the reflector is far from the auxiliary passive array, can be approximated by

$$
(3.6) \qquad \hat{u}_0(\omega, \vec{\boldsymbol{y}}; \vec{\boldsymbol{x}}_s) = -2i\frac{\omega}{c_0} \int_{\mathbb{R}^2} \hat{u}_0(\omega, (\boldsymbol{x}, -L); \vec{\boldsymbol{x}}_s) \hat{G}_0(\omega, (\boldsymbol{x}, -L); \vec{\boldsymbol{y}}) d\boldsymbol{x}.
$$

Substituting (3.6) into (3.5) gives (3.3).

4. The mean imaging function. From now on we assume that the auxiliary receiver array is a regular grid that covers the region $[-a/2, a/2]^2 \times \{-L\}$, and we denote by ΔX_{q} the grid mesh size, with $a^2/\Delta X_{\mathrm{q}}^2 = N_{\mathrm{q}}$. Similarly, we assume that the source array is a regular grid that covers the region $[-b/2, b/2]^2 \times \{0\}$, and we denote by ΔX_{s} the grid mesh size, with $b^2/\Delta X_{\mathrm{s}}^2 = N_{\mathrm{s}}$. Recall that the support of the Fourier transform $\hat{F}(\omega)$ of the source in the positive frequencies is $[\omega_0 - B/2, \omega_0 + B/2]$. Here ω_0 is the central frequency and $\lambda_0 = 2\pi c_0/\omega_0$ is the central wavelength of the source. The following proposition (proved in Appendix A) gives the full expression of the expectation of the imaging function, from which we can determine the resolution of the image.

Proposition 4.1. *We consider the regime in which $X_{\mathrm{cq}} \ll a \ll L_y - L$. We also assume $c_0/B \ll (L_y - L)$ and $\Delta X_{\mathrm{q}} \ll \lambda_0(L_y - L)/a$. We express the search point near the reflector as $\vec{\boldsymbol{y}}^S = (\boldsymbol{y} + \boldsymbol{\xi}, -L_y - \eta)$. The mean imaging function is given by*

$$
(4.1) \qquad
\begin{aligned}
\mathbb{E}\big[\mathcal{I}_{\mathrm{CC}}(\vec{\boldsymbol{y}}^S)\big] = {} & \frac{N_{\mathrm{s}} N_{\mathrm{q}}^2}{a^4} \frac{\sigma_{\mathrm{ref}} X_{\mathrm{cq}}^2}{8\pi c_0^3 (L_y - L)^2} \int_{\mathbb{R}} (-i\omega^3) |\hat{F}(\omega)|^2 \exp\left(-2i\frac{\omega}{c_0}\eta\right) \\
& \times \left[\int_{[-a/2, a/2]^2} \exp\left(i\frac{\omega \boldsymbol{\xi} \cdot (\boldsymbol{x}_{q'} - \boldsymbol{y})}{c_0(L_y - L)}\right) d\boldsymbol{x}_{q'} \right] \\
& \times \left[\int_{[-a/2, a/2]^2} \exp\left(-\frac{X_{\mathrm{cq}}^2 \omega^2 |\boldsymbol{x}_q - \boldsymbol{y}|^2}{4c_0^2(L_y - L)^2} + i\frac{\omega \boldsymbol{\xi} \cdot (\boldsymbol{x}_q - \boldsymbol{y})}{c_0(L_y - L)}\right) d\boldsymbol{x}_q \right] d\omega.
\end{aligned}
$$

We can briefly comment on the hypotheses of Proposition 4.1. The small aperture hypothesis $a \ll L_y - L$ leads to the paraxial approximation that simplifies the expressions but does not qualitatively change the results. The hypothesis $X_{\mathrm{cq}} \ll a$ is the minimal hypothesis that ensures that the field can be considered as spatially uncorrelated across the auxiliary receiver array. The hypothesis $c_0/B \ll (L_y - L)$ means that the pulse width is smaller than the travel time from the auxiliary receiver array to the reflector, which is the minimal hypothesis needed to have some range information in the recorded data. The hypothesis $\Delta X_{\mathrm{q}} \ll \lambda_0(L_y - L)/a$ allows us to use the continuum approximation for the sums over $\boldsymbol{x}_q, \boldsymbol{x}_{q'}$, which become integrals over $[-a/2, a/2]^2$ in (4.1).

The following proposition is straightforward and provides a simple form for the point spread function (the imaging function for a point reflector) from which the resolution of the image is assessed. The expression of the peak amplitude of the imaging function will be used when we study the SNR of the image in the next section.

Proposition 4.2. *We assume the same hypotheses as in Proposition 4.1 and additionally that $B \ll \omega_0$. If we consider that the reflector location is $\vec{\boldsymbol{y}} = (\boldsymbol{0}, -L_y)$, then we have the following results for the search point $\vec{\boldsymbol{y}}^S = (\boldsymbol{\xi}, -L_y - \eta)$.*

1. *If $X_{\mathrm{cq}} \ll \lambda_0(L_y - L)/a$, then*

$$\mathbb{E}\big[\mathcal{I}_{\mathrm{CC}}(\vec{\boldsymbol{y}}^S)\big] = -\frac{N_{\mathrm{s}} N_{\mathrm{q}}^2 \sigma_{\mathrm{ref}} \omega_0^3 X_{\mathrm{cq}}^2}{4\pi c_0^3 (L_y - L)^2}\left[\int_0^\infty |\hat{F}(\omega)|^2 \sin\left(2\frac{\omega}{c_0}\eta\right) d\omega\right]$$

(4.2)
$$\times\ \mathrm{sinc}^2\left(\frac{\omega_0 a \xi_1}{c_0(L_y - L)}\right)\mathrm{sinc}^2\left(\frac{\omega_0 a \xi_2}{c_0(L_y - L)}\right).$$

2. *If $X_{\mathrm{cq}} \gg \lambda_0(L_y - L)/a$, then*

$$\mathbb{E}\big[\mathcal{I}_{\mathrm{CC}}(\vec{\boldsymbol{y}}^S)\big] = -\frac{N_{\mathrm{s}} N_{\mathrm{q}}^2 \sigma_{\mathrm{ref}} \omega_0}{a^2 c_0}\left[\int_0^\infty |\hat{F}(\omega)|^2 \sin\left(2\frac{\omega}{c_0}\eta\right) d\omega\right]$$

(4.3)
$$\times\ \mathrm{sinc}\left(\frac{\omega_0 a \xi_1}{c_0(L_y - L)}\right)\mathrm{sinc}\left(\frac{\omega_0 a \xi_2}{c_0(L_y - L)}\right).$$

The sinc function is defined by $\mathrm{sinc}(s) = \sin(s)/s$. Here we used the fact that $\omega \to |\hat{F}(\omega)|^2$ is an even function since $t \to F(t)$ is real-valued.

The hypothesis $B \ll \omega_0$ allows us to simplify the expression (4.1) of the mean imaging function by approximating the ω-integrated transverse spatial profile (in $\boldsymbol{\xi}$) by its value at $\omega = \omega_0$, which gives the sinc functions with radius $\lambda_0(L_y - L)/a$. If $\hat{F}(\omega) = \mathbf{1}_{[\omega_0 - B/2, \omega_0 + B/2]}(|\omega|)$, then the longitudinal profile (in η) is also a sinc function, with radius c_0/B, modulated by a rapid sin function:

$$\int_0^\infty |\hat{F}(\omega)|^2 \sin\left(2\frac{\omega}{c_0}\eta\right) d\omega = B\,\mathrm{sinc}\left(\frac{B\eta}{c_0}\right)\sin\left(\frac{2\omega_0\eta}{c_0}\right).$$

Proposition 4.2 shows that the cross-range resolution is $\lambda_0(L_y - L)/a$ and the range resolution is c_0/B. These resolution formulas are the classical Rayleigh resolution limits obtained with active arrays in a homogeneous medium [10].

We note the existence of two regimes: (1) When $X_{\mathrm{cq}} \gg \lambda_0(L_y - L)/a$, which means that the transverse correlation radius of the illumination field on the auxiliary passive array is quite large, then the point spread function of the image has the form of a simple sinc function. It is as if we were using a single, coherent (say plane wave) illumination towards the reflector and we were migrating the auxiliary receiver array data vector to form an image. (2) When $X_{\mathrm{cq}} \ll \lambda_0(L_y - L)/a$, which means that the transverse correlation radius of the illumination field on the auxiliary passive array is quite small, then the point spread function has the form of a sinc^2 function. This is as if the sensors of the auxiliary receiver array were used as active point sources emitting towards the reflector and we were migrating the full response matrix of the array to form an image. This shows that the decorrelation properties of the illumination field at the auxiliary passive array play an essential role, as they allow the quantification of the diversity of the illumination.

Note also that, in the situation addressed in this paper, we get a better image than if we were using the response matrix of an active array of point sources that would emit in all directions from the auxiliary array location. In such a case we would have contributions from

waves emitted towards the surface and backscattered by the medium. In our situation the cross correlation matrix only contains the contributions of waves going towards the reflector and reflected by it, and not the incoherent contributions backscattered from the random medium. This does not affect resolution but it affects the statistical stability.

We also note that the sensor density of the auxiliary receiver array plays no role in the resolution of the imaging function (provided $\Delta X_q \ll \lambda_0 (L_y - L)/a$). However, we will see in section 6 that it plays a role in the statistical stability of the image.

5. Connection with the random paraxial regime. In the previous section, Propositions 4.1 and 4.2 regarding resolution were derived using the Kronecker model. In this section we show that the same results, which rely on second moments only, can be obtained from a multiscale analysis starting from the wave equation in the random paraxial regime. The comparison of these two sets of results shows that the Kronecker model can be calibrated so as to give the same resolution results in correlation-based imaging as those in the random paraxial regime. As pointed out is section 3.1, this is not so for the fourth moments, and therefore for SNR calculations. In more detail, we relate the parameter X_{cq} of the Kronecker model to the physical parameters of the random paraxial model in subsection 5.1. In subsection 5.2 we compare the results obtained in this paper with those obtained in [19] using a multiscale analysis in the random paraxial regime, and we show that the two sets of results are equivalent upon the suitable identification of the parameter X_{cq} of the Kronecker model.

5.1. The form of the covariance function. The form (3.2) of the field covariance function has been derived in different situations in which scattering is relatively strong. In particular it was derived in the random paraxial regime in [5, Appendix B] and in [11, 12]. Without reproducing the full analysis, we can briefly examine the dependence of the covariance function with respect to the receiver offset in the case of a medium with isotropic three-dimensional weak fluctuations $\mu(\vec{x})$ of the index of refraction. When the conditions for the paraxial approximation are fulfilled, backscattering can be neglected, and wave propagation is governed by an Itô–Schrödinger equation [20],

$$d\hat{u}_0(\boldsymbol{x}, z) = \frac{ic_0}{2\omega}\Delta_{\boldsymbol{x}}\hat{u}_0(\boldsymbol{x}, z)dz + \frac{i\omega}{2c_0}\hat{u}_0(\boldsymbol{x}, z) \circ dW(\boldsymbol{x}, z), \qquad (\boldsymbol{x}, z) \in \mathbb{R}^2 \times (-\infty, 0),$$

with the initial condition in the plane $z = 0$: $\hat{u}_0(\boldsymbol{x}, z = 0) = -\delta(\boldsymbol{x} - \boldsymbol{x}_s)/2$. Here the symbol $\circ$ stands for the Stratonovich stochastic integral and $W(\boldsymbol{x}, z)$ is a real-valued zero-mean Gaussian field with covariance function given by

$$(5.1) \qquad \mathbb{E}\big[W(\boldsymbol{x}, z)W(\boldsymbol{x}', z')\big] = \gamma_0(\boldsymbol{x} - \boldsymbol{x}') \min\big\{|z|, |z'|\big\},$$

with

$$(5.2) \qquad \gamma_0(\boldsymbol{x}) = \int_{-\infty}^{\infty} \mathbb{E}[\mu(\boldsymbol{0}, 0)\mu(\boldsymbol{x}, z)]dz.$$

The first two moments of the field transmitted through the random medium in $z \in (-L, 0)$ have the following expressions at the auxiliary receiver array:

$$(5.3) \qquad \mathbb{E}\big[\hat{u}_0(\omega, \vec{\boldsymbol{x}}_q)\big] = \hat{u}_{\text{homo}}(\omega, \vec{\boldsymbol{x}}_q) \exp\Big(-\frac{\gamma_0(\boldsymbol{0})\omega^2 L}{8c_0^2}\Big),$$

where γ_0 is given by (5.2) and $\hat{u}_{\text{homo}}$ is the solution in the homogeneous medium, and

$$(5.4) \qquad \mathbb{E}\left[\hat{u}_0(\omega, \vec{\boldsymbol{x}}_q)\overline{\hat{u}_0(\omega, \vec{\boldsymbol{x}}_{q'})}\right] = \hat{u}_{\text{homo}}(\omega, \vec{\boldsymbol{x}}_q)\overline{\hat{u}_{\text{homo}}(\omega, \vec{\boldsymbol{x}}_{q'})}\exp\left(-\frac{\gamma_2(\boldsymbol{x}_q - \boldsymbol{x}_{q'})\omega^2 L}{4c_0^2}\right),$$

where $\gamma_2(\boldsymbol{x}) = \int_0^1 \gamma_0(\boldsymbol{0}) - \gamma_0(\boldsymbol{x}s)ds$. These are classical results (see [22, Chapter 20] and [19]) once the Itô–Schrödinger equation has been proved to be correct. In the case in which scattering is strong so that $\gamma_0(\boldsymbol{0})\omega_0^2 L/(8c_0^2)$ becomes larger than one, the first moment (5.3) is vanishing and the second moment (5.4) takes the form

$$\mathbb{E}\left[\hat{u}_0(\omega, \vec{\boldsymbol{x}}_q)\overline{\hat{u}_0(\omega, \vec{\boldsymbol{x}}_{q'})}\right] = \hat{u}_{\text{homo}}(\omega, \vec{\boldsymbol{x}}_q)\overline{\hat{u}_{\text{homo}}(\omega, \vec{\boldsymbol{x}}_{q'})}\exp\left(-\frac{|\boldsymbol{x}_q - \boldsymbol{x}_{q'}|^2}{X_{\text{cq}}^2}\right)$$

for any $\omega \in [\omega_0 - B/2, \omega_0 + B/2]$, where X_{cq} given by

$$(5.5) \qquad\qquad\qquad X_{\text{cq}}^2 = \frac{12c_0^2}{\bar{\gamma}_2\omega_0^2 L} = \frac{3\lambda_0^2}{\pi^2\bar{\gamma}_2 L}$$

is the correlation radius of the field at the auxiliary receiver array, $\lambda_0 = 2\pi c_0/\omega_0$ is the central wavelength, and $\bar{\gamma}_2$ comes from the expansion $\gamma_0(\boldsymbol{x}) = \gamma_0(\boldsymbol{0}) - \bar{\gamma}_2|\boldsymbol{x}|^2 + o(|\boldsymbol{x}|^2)$.

The form (3.2) of the field covariance function was also obtained (along with higher-order moments) with a simpler model of the random medium, the so-called random travel time model, that affects only the phases and gives random wave front distortions [4]. In this model, the field in the random medium is the unperturbed field with an additional random phase whose standard deviation is much larger than 2π. This large phase explains why the mean field is zero. The large phases in the product of fields in the covariance function compensate each other, because one of the fields is complex-conjugated, and this compensation happens only when the frequencies and the receivers are close to each other. This explains the form of the covariance function (3.2).

5.2. The form of the imaging function. We give a brief review of the results that can be found in [19] that give the expression of the mean imaging function in the random paraxial regime and compare them with the results of Proposition 4.2.

At the end of section 3.4 of [19], we find the very same results as in Proposition 4.2 if we take care to identify the effective receiver aperture a_{eff} defined in section 3.4 of [19] (see Figure 2) with $\lambda_0(L_y - L)/X_{\text{cq}}$. According to section 3.4 of [19], the effective receiver aperture a_{eff} is the diameter of the piece of the auxiliary receiver array that is effectively used in imaging the reflector just below it. The identification of a_{eff} with $\lambda_0(L_y - L)/X_{\text{cq}}$ makes sense because a field with angular diversity in a cone with width λ_0/X_{cq} and with an offset larger than a_{eff} will not illuminate the reflector at distance $L_y - L$, while a beam with an offset smaller than a_{eff} will illuminate the reflector.

The two cases identified in Proposition 4.2, i.e., $X_{\text{cq}} \ll \lambda_0(L_y - L)/a$ (resp., $X_{\text{cq}} \gg \lambda_0(L_y - L)/a$), correspond to $a_{\text{eff}} \gg a$ (resp., $a_{\text{eff}} \ll a$), as stated at the end of section 3.4 of [19], where we had already identified the two regimes with sinc or sinc^2. The results are again in agreement.

(a) Homogeneous medium.   (b) Random medium.
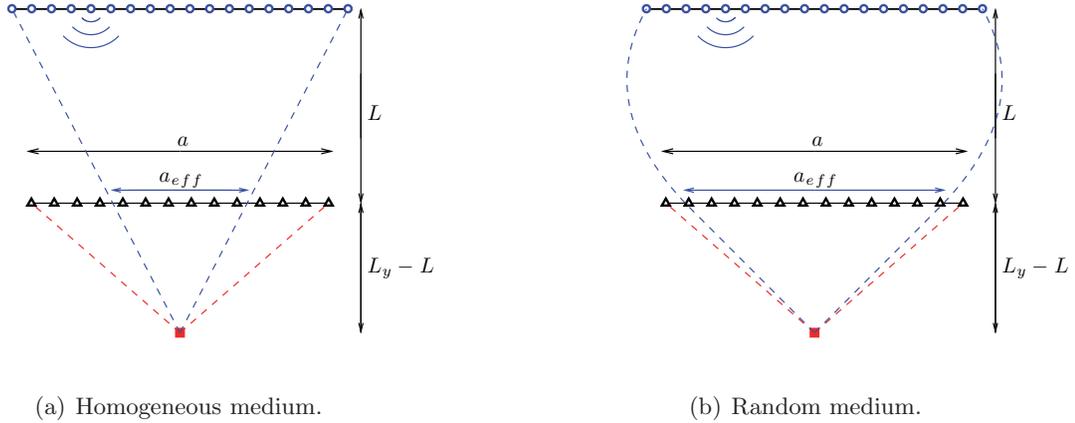
Figure 2. *Effective receiver aperture a_{eff} in a homogeneous medium* (a) *and in a random medium* (b). *Scattering enhances illumination diversity and increases the effective receiver aperture.*

Furthermore, since $a_{\text{eff}} \simeq \bar{\gamma}_2^{1/2} L^{3/2}(L_y - L)/L_y \simeq \bar{\gamma}_2^{1/2} L^{1/2}(L_y - L)$ (see equations (2.3)–(2.4) in [19]), we can again identify $X_{\text{cq}} \simeq \lambda_0/(\bar{\gamma}_2^{1/2} L^{1/2})$ as in (5.5).

These resolution estimates, obtained on the one hand with the paraxial wave model, and on the other hand with the Kronecker model, are thus fully consistent with each other. This shows that the Kronecker model can be used without loss of precision in estimating resolution in virtual source imaging. This is not so surprising because the strong scattering between the source array and the auxiliary receiver array helps to diversify the effective illumination incident on the reflector to be imaged. Since the region between the auxiliary receiver array and the reflector is assumed homogeneous, the resolution of the image is beneficially affected by the scattering when imaging with cross correlations, as seen in Figure 2.

6. Statistical stability of the imaging function. We now address the statistical stability of the image, which is the main objective of this paper. We will get an approximate formula for what we call the signal-to-noise ratio (SNR) defined as the mean imaging function at the reflector position over the standard deviation of the imaging function:

$$(6.1) \qquad \text{SNR}_{\text{CC}} = \frac{|\mathbb{E}[\mathcal{I}_{\text{CC}}(\vec{\boldsymbol{y}})]|}{\text{Var}(\mathcal{I}_{\text{CC}}(\vec{\boldsymbol{y}}^S))^{1/2}}$$

for $\vec{\boldsymbol{y}}^S$ in the vicinity of $\vec{\boldsymbol{y}}$. This is not what is usually called SNR, the ratio of signal to noise energy, since there is no source of noise energy here. But the medium inhomogeneities do create fluctuations in the wave fields and hence in the signals received by the auxiliary array, and so (6.1) does measure the relative size of the fluctuations in the image much as in the usual SNR. The following proposition is proved in Appendix B and describes the variance of the imaging function as a function of the parameters of the problem.

Proposition 6.1. *We assume the same hypotheses as in Proposition* 4.1 *and additionally* $b \gg X_{\mathrm{cs}}$ *and* $\omega_{\mathrm{c}} \ll B$. *We consider a search point* $\vec{y}^S$ *in the vicinity of* $\vec{y}$. *We denote*

$$
(6.2) \qquad I_{\mathrm{s}} = \sum_{s,s'=1}^{N_{\mathrm{s}}} \exp\left(-\frac{2|\boldsymbol{x}_s - \boldsymbol{x}_{s'}|^2}{X_{\mathrm{cs}}^2}\right).
$$

1. *If* $\Delta X_{\mathrm{q}} \gg X_{\mathrm{cq}}$, *then*

$$
(6.3) \qquad \mathrm{Var}\big(\mathcal{I}_{\mathrm{CC}}(\vec{y}^S)\big) = I_{\mathrm{s}} N_{\mathrm{q}}^2 \frac{\pi^{1/2}}{2^{1/2}} \omega_{\mathrm{c}} \left[\int |\hat{F}(\omega)|^4 d\omega\right].
$$

2. *If* $\Delta X_{\mathrm{q}} \ll X_{\mathrm{cq}}$ *and* $X_{\mathrm{cq}} \ll \lambda_0(L_y - L)/a$, *then*

$$
(6.4) \qquad \mathrm{Var}\big(\mathcal{I}_{\mathrm{CC}}(\vec{y}^S)\big) = \frac{I_{\mathrm{s}} N_{\mathrm{q}}^2}{\Delta X_{\mathrm{q}}^4} \frac{\pi^{5/2}\omega_{\mathrm{c}} X_{\mathrm{cq}}^4}{2^{1/2}} \left[\int |\hat{F}(\omega)|^4 d\omega\right].
$$

3. *If* $\Delta X_{\mathrm{q}} \ll X_{\mathrm{cq}}$ *and* $X_{\mathrm{cq}} \gg \lambda_0(L_y - L)/a$, *then*

$$
(6.5) \qquad \mathrm{Var}\big(\mathcal{I}_{\mathrm{CC}}(\vec{y}^S)\big) = \frac{I_{\mathrm{s}}}{\Delta X_{\mathrm{q}}^8} \frac{2^{7/2}\pi^{9/2}\omega_{\mathrm{c}} c_0^4 (L_y - L)^4}{\omega_0^4} \left[\int |\hat{F}(\omega)|^4 d\omega\right].
$$

This proposition shows in particular that the ratio of the distance between receivers ΔX_{q} on the auxiliary array and the correlation radius of the illumination field X_{cq} plays an important role in the variance of the fluctuations of the image. By combining the results of Propositions 4.2 and 6.1, we get the following result (see Appendix C). Recall that $N_{\mathrm{s}}^{1/2}\Delta X_{\mathrm{s}} = b$ is the source array aperture and $N_{\mathrm{q}}^{1/2}\Delta X_{\mathrm{q}} = a$ is the auxiliary receiver array aperture.

Proposition 6.2. *As a function of the interdistance between receivers* ΔX_{q}, *the interdistance between sources* ΔX_{s}, *and the bandwidth of the source* B, *the SNR varies as*

$$
(6.6) \qquad \mathrm{SNR}_{\mathrm{CC}} \approx \frac{\sigma_{\mathrm{ref}} X_{\mathrm{cq}}^2}{\lambda_0^3 (L_y - L)^2}\left(\frac{b}{\max\{\Delta X_{\mathrm{s}}, X_{\mathrm{cs}}\}}\right)\left(\frac{a}{\max\{\Delta X_{\mathrm{q}}, X_{\mathrm{cq}}\}}\right)^2 \left(\frac{B}{\omega_{\mathrm{c}}}\right)^{1/2}.
$$

This proposition shows that, when the correlation radius X_{cq} is small, then it is relevant to have a dense auxiliary receiver array for a given aperture in order to get good stability. Indeed, for a given aperture a, the SNR increases when the interdistance ΔX_{q} decreases, until the interdistance becomes of the order of the correlation radius X_{cq} of the illumination field, and then the SNR reaches a value determined by X_{cq}. Proposition 6.2 is the main theoretical result of this paper. It is supported well by direct numerical simulations as we describe in the next section.

7. Numerical simulations. We consider a two-dimensional imaging setup as shown in Figure 3. We use parameters that are similar to those in exploration geophysics, but with somewhat higher frequencies. The reflector that we wish to image is situated below a complex structure, modeled here by random fluctuations in the speed of propagation $c(\vec{x})$ given by (2.4). The fluctuations of the velocity, μ, are obtained by combining an isotropic and a layered random process,

$$
(7.1) \qquad \mu(\vec{x}) = \frac{\sigma}{\sqrt{2}}\left(\mu_i(\vec{x}) + \mu_l(\vec{x})\right),
$$

with standard deviation $\sigma = 0.08$. The isotropic part $\mu_i(\vec{x})$ has a Gaussian correlation function

$$E\big[\mu_i(\vec{x}_1)\mu_i(\vec{x}_2)\big] = \exp\Big(-\frac{|\vec{x}_1 - \vec{x}_2|^2}{2\ell^2}\Big), \qquad \ell = \lambda_0/2,$$

and the layered random process $\mu_l(\vec{x})$ satisfies

$$E\big[\mu_l((x_1, z_1))\mu_l((x_2, z_2))\big] = \Big(1 + \frac{|z_1 - z_2|}{\ell_z}\Big)\exp\Big(-\frac{|z_1 - z_2|}{\ell_z}\Big), \qquad \ell_z = \lambda_0/30.$$

In Figure 3 we plot the square of the sound speed that fluctuates around the constant $c_0 = 3000$m/s. The reflector is modeled by a square centered at $(0, -60\lambda_0)$ with edge length equal to $2\lambda_0$ and a homogeneous Dirichlet condition on its boundary.

At the free-surface at the top of the computational domain we use a Neumann boundary condition, and we also have an array of $N_s = 97$ sources-receivers located at $\vec{x}_s = (-24\lambda_0 + (s-1)\lambda_0/2, 0)$, $s = 1, \ldots, N_s$. We assume that we can record the pressure field on an auxiliary array of $N_q = 61$ receivers located at $\vec{x}_q = (-15\lambda_0 + (q-1)\lambda_0/2, -51\lambda_0)$, $q = 1, \ldots, N_q$. The simulation that we do is as follows. From each source located at the surface array we send a pulse of the form

$$(7.2) \qquad\qquad F(t) = \mathrm{sinc}(B_0 t)\cos(2\pi f_0 t)\exp\Big(-\frac{t^2}{2T_0^2}\Big),$$

and we record the response at the auxiliary receiver array that is located below the complex structure of the medium. In (7.2) we take $f_0 = 100\,\mathrm{Hz}$, $B_0 = 100\,\mathrm{Hz}$, and $T_0 = 0.3\,\mathrm{s}$ so that $\lambda_0 = 30\,\mathrm{m}$.

The Fourier transform of the pulse is supported in the frequency interval $[f_0 - \Delta f/2, f_0 + \Delta f/2] = [80, 120]\,\mathrm{Hz}$ for $f_0 = 100\,\mathrm{Hz}$ and $\Delta f = 40\,\mathrm{Hz}$.

To summarize, in the numerical simulations we have a central wavelength $\lambda_0 = 30$m, and the values for the different length scales that appear in the analysis are as follows: $L = 51\lambda_0$, the distance between the source array and the auxiliary array; $L_y = 60\lambda_0$, the distance between the reflector and the source array; $a = 30\lambda_0$, the aperture of the auxiliary array; and $b = 48\lambda_0$, the aperture of the source array.

7.1. Kirchhoff migration imaging. Let us first consider what happens when the array at the surface is used as a receiver array as well. We display in Figure 4(a) the traces recorded on the array as a function of distance from the source $\vec{x}_1$ and in Figure 4(b) the Kirchhoff migration (KM) image obtained when using all sources on the array. Recall that the KM image obtained at a search point $\vec{y}^S$, considering the receivers located at $(\vec{x}_r)_{1 \le r \le N_r}$ (both sources and receivers are located on the surface), is

$$(7.3) \qquad\qquad \mathcal{I}_{\mathrm{KMr}}(\vec{y}^S) = \sum_{s=1}^{N_s}\sum_{r=1}^{N_r} u\big(\mathcal{T}(\vec{x}_s, \vec{y}^S) + \mathcal{T}(\vec{x}_r, \vec{y}^S), \vec{x}_r; \vec{x}_s\big).$$

In Figure 4(a), we see that the traces are strongly fluctuating and the reflected signal from the object that we wish to image is overwhelmed by the multiple scattering from the complex
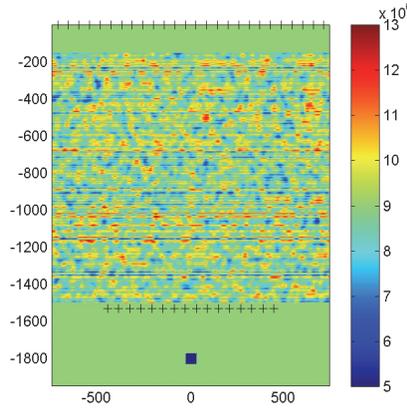
Figure 3. *The imaging setup. The reflector that we wish to image is below the complex medium. We have two arrays, an active one on the surface and a passive one below the complex structure. The axes are in meters.*
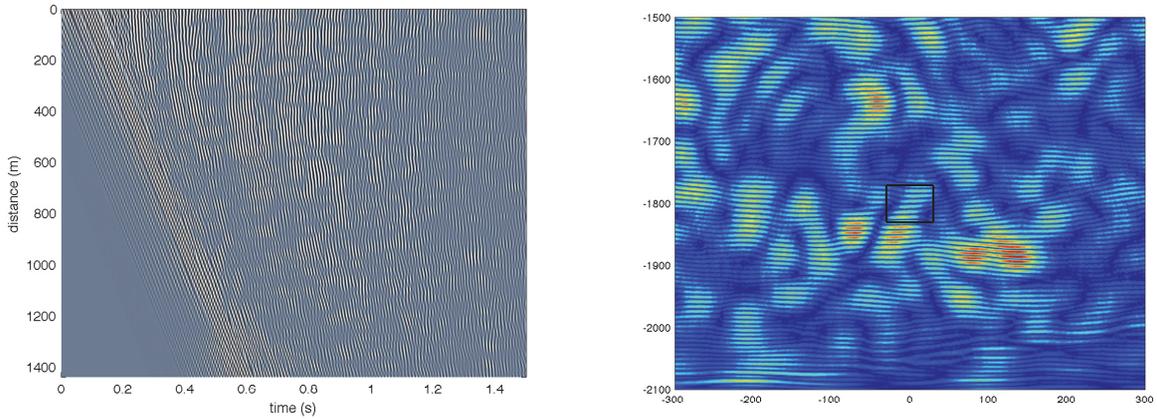
(a) Traces on the surface receiver array. Each line is the trace recorded by one receiver.

(b) KM image $\mathcal{I}_{\mathrm{KMr}}$.

Figure 4. *Traces and Kirchhoff migration image $\mathcal{I}_{\mathrm{KMr}}$ using the data of the surface receiver array.*

medium. The corresponding KM image is also very noisy. It is clear that in such a medium we cannot image the reflector using the array at the surface.

Another image that we can compute is the KM image considering the receivers located on the auxiliary array at $(\vec{\boldsymbol{x}}_q)_{1 \leq q \leq N_{\mathrm{q}}}$. With the sources at the surface but with the receivers inside the medium at the auxiliary array, the imaging function is given by

$$(7.4) \qquad \mathcal{I}_{\mathrm{KM}}(\vec{\boldsymbol{y}}^S) = \sum_{s=1}^{N_{\mathrm{s}}} \sum_{q=1}^{N_{\mathrm{q}}} u\big(\mathcal{T}(\vec{\boldsymbol{x}}_s, \vec{\boldsymbol{y}}^S) + \mathcal{T}(\vec{\boldsymbol{x}}_q, \vec{\boldsymbol{y}}^S), \vec{\boldsymbol{x}}_q; \vec{\boldsymbol{x}}_s\big).$$

We show in Figure 5(a) the traces recorded on the auxiliary receiver array (for source $\vec{\boldsymbol{x}}_1$) and in Figure 5(b) the KM image $\mathcal{I}_{\mathrm{KM}}$. The results are poor as well, and we cannot obtain

(a) Traces on the auxiliary receiver array.
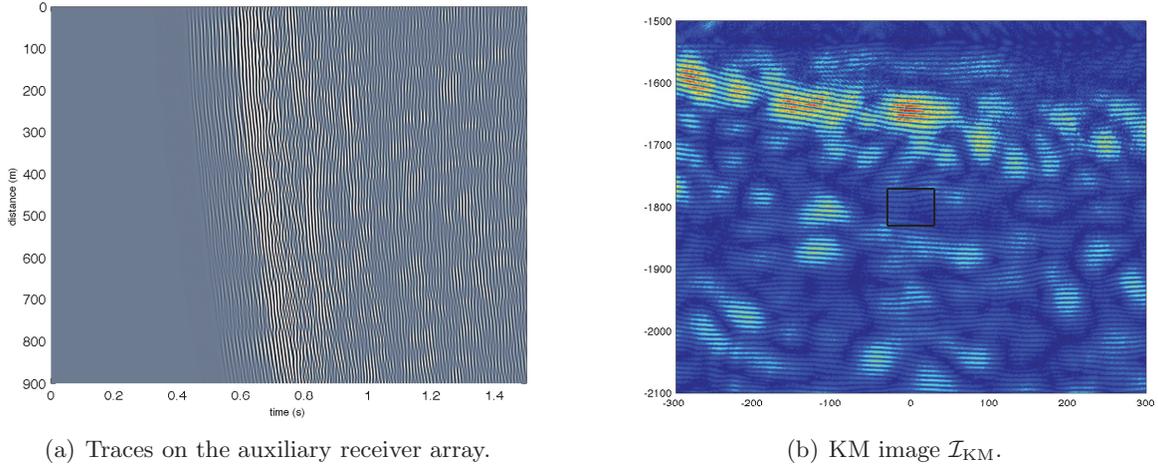
(b) KM image $\mathcal{I}_{\mathrm{KM}}$.

Figure 5. *Traces and Kirchhoff migration image $\mathcal{I}_{\mathrm{KM}}$ using the data of the auxiliary receiver array.*

a good image of the reflector. Note that the Kronecker model predicts that the mean wave is zero, so that the SNR of the KM image is theoretically zero. In a more reasonable model, such as the random paraxial model [19] or the random travel time model [4], the mean wave (and therefore the mean KM imaging function) is exponentially small as a function of the propagation distance, which gives a very low SNR for the image.

7.2. Imaging with cross correlations of the surface array data. Let us consider imaging with cross correlations of the recorded traces at the surface array $(\vec{\boldsymbol{x}}_r)_{1 \leq r \leq N_{\mathrm{r}}}$. We compute the following imaging function:

$$(7.5) \qquad \mathcal{I}_{\mathrm{CCr}}\big(\vec{\boldsymbol{y}}^S\big) = \sum_{r,r'=1}^{N_{\mathrm{r}}} \mathcal{C}_{\mathrm{r}}\big(\mathcal{T}(\vec{\boldsymbol{y}}^S, \vec{\boldsymbol{x}}_r) + \mathcal{T}(\vec{\boldsymbol{y}}^S, \vec{\boldsymbol{x}}_{r'}), \vec{\boldsymbol{x}}_r, \vec{\boldsymbol{x}}_{r'}\big),$$

with the cross correlation $\mathcal{C}_{\mathrm{r}}(\tau, \vec{\boldsymbol{x}}_r, \vec{\boldsymbol{x}}_{r'})$ computed by

$$(7.6) \qquad \mathcal{C}_{\mathrm{r}}(\tau, \vec{\boldsymbol{x}}_r, \vec{\boldsymbol{x}}_{r'}) = \sum_{s=1}^{N_{\mathrm{s}}} \int u(t, \vec{\boldsymbol{x}}_r; \vec{\boldsymbol{x}}_s) u(t + \tau, \vec{\boldsymbol{x}}_{r'}; \vec{\boldsymbol{x}}_s) dt.$$

We show in Figure 6(a) the cross correlations on the surface array $\mathcal{C}_{\mathrm{r}}(\tau, \vec{\boldsymbol{x}}_r, \vec{\boldsymbol{x}}_1)$, $r = 1, \ldots, N_{\mathrm{r}}$ and in Figure 6(b) the image $\mathcal{I}_{\mathrm{CCr}}$. The low quality of the image is clearly visible.

We show in Figure 7 the image computed using the cross correlations on the surface receiver array when only the diagonal terms are taken into account; i.e., we compute

$$(7.7) \qquad \mathcal{I}_{\mathrm{CCr}}^{\mathrm{diag}}(\vec{\boldsymbol{y}}^S) = \sum_{r=1}^{N_{\mathrm{r}}} \mathcal{C}_{\mathrm{r}}\big(2\mathcal{T}(\vec{\boldsymbol{y}}^S, \vec{\boldsymbol{x}}_r), \vec{\boldsymbol{x}}_r, \vec{\boldsymbol{x}}_r\big),$$

with the cross correlation term $\mathcal{C}_{\mathrm{r}}(\tau, \vec{\boldsymbol{x}}_r, \vec{\boldsymbol{x}}_{r'})$ computed as before by (7.6). Again the low quality of this image is clearly visible.

(a) Cross correlations on the surface array.
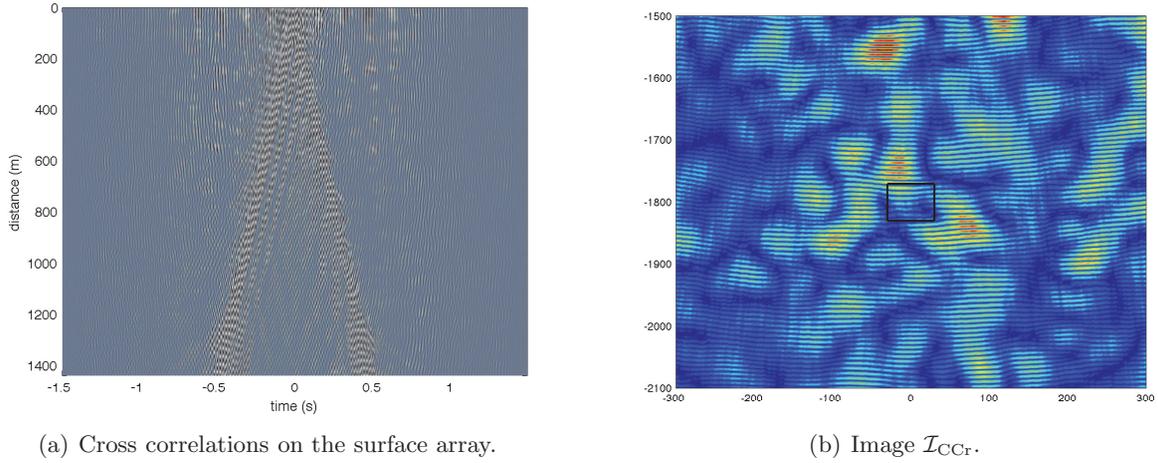
(b) Image $\mathcal{I}_{\mathrm{CCr}}$.

Figure 6. *Cross correlations and image $\mathcal{I}_{\mathrm{CCr}}$ using the data of the surface array.*
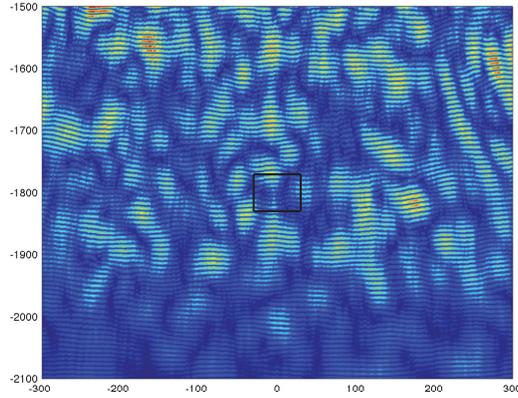
Figure 7. *Image $\mathcal{I}_{\mathrm{CCr}}^{\mathrm{diag}}$ using the data of the surface array.*

7.3. Imaging with cross correlations of the auxiliary array data. Let us consider imaging with cross correlations of the recorded traces at the auxiliary array $(\vec{\boldsymbol{x}}_q)_{1 \leq q \leq N_{\mathrm{q}}}$. We display in Figure 8(a) the cross correlations on the auxiliary receiver array $\mathcal{C}(\tau, \vec{\boldsymbol{x}}_q, \vec{\boldsymbol{x}}_1)$, $q = 1, \ldots, N_{\mathrm{q}}$, and in Figure 8(b) the image $\mathcal{I}_{\mathrm{CC}}$ defined by (2.5). Comparing the images shown in Figures 6(b) and 8(b) it is easy to conclude that the best imaging functional is $\mathcal{I}_{\mathrm{CC}}$ that uses cross correlations on the auxiliary receiver array.

Finally, a natural question that arises is what happens if we compute the imaging functional using relation (2.5), with the cross correlation term $\mathcal{C}(\tau, \vec{\boldsymbol{x}}_q, \vec{\boldsymbol{x}}_{q'})$ computed by

$$(7.8) \qquad \mathcal{C}(\tau, \vec{\boldsymbol{x}}_q, \vec{\boldsymbol{x}}_{q'}) = \int \left(\sum_{s=1}^{N_{\mathrm{s}}} u(t, \vec{\boldsymbol{x}}_q; \vec{\boldsymbol{x}}_s) \right) \left(\sum_{s=1}^{N_{\mathrm{s}}} u(t + \tau, \vec{\boldsymbol{x}}_{q'}; \vec{\boldsymbol{x}}_s) \right) dt.$$

We plot in Figure 9(b) the imaging functional $\mathcal{I}_{\mathrm{CC}}$ computed with cross correlations given by (7.8), and we compare it with $\mathcal{I}_{\mathrm{CC}}$ plotted in Figure 9(a). It is clear that the quality

(a) Cross correlations on the auxiliary receiver array.   (b) Image $\mathcal{I}_{\mathrm{CC}}$.
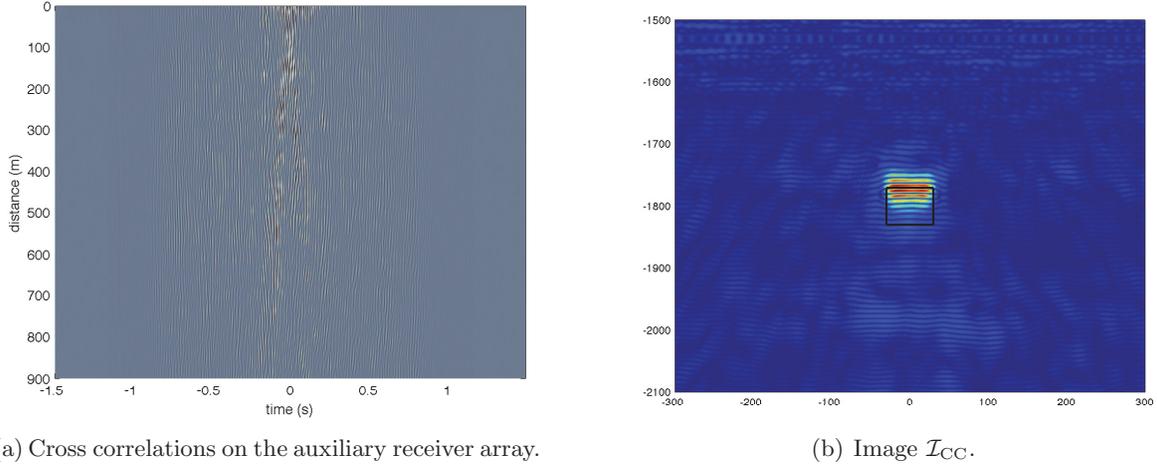
Figure 8. *Cross correlations and image $\mathcal{I}_{\mathrm{CC}}$ using the data of the auxiliary receiver array.*

(a) Plot of $\mathcal{I}_{\mathrm{CC}}$.   (b) Plot of $\mathcal{I}_{\mathrm{CC}}$ when cross correlations are computed with crossed terms.
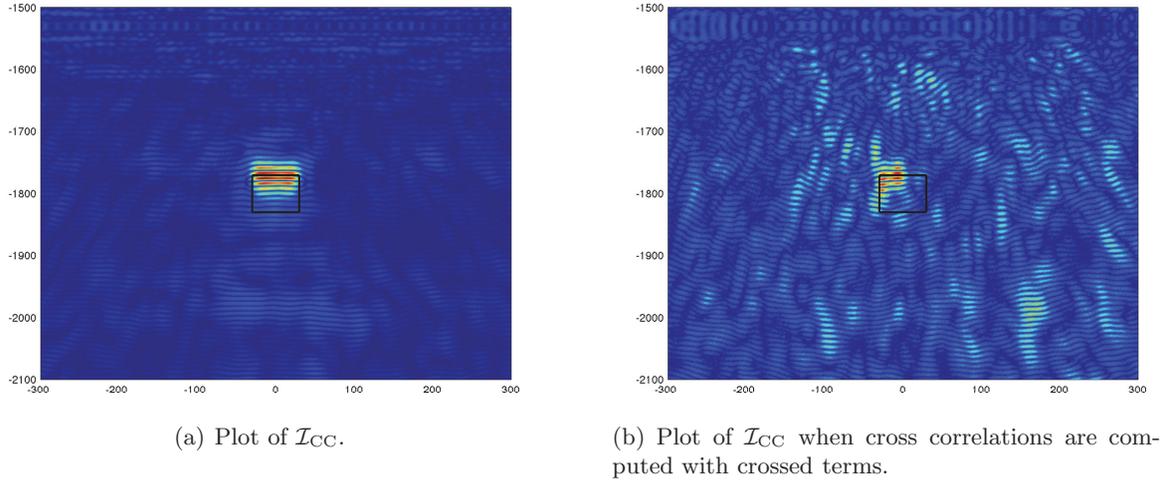
Figure 9. *Comparison between $\mathcal{I}_{\mathrm{CC}}$ images using (2.6) for computing the cross correlations on the left and (7.8) on the right.*

of the image deteriorates when the crossed terms $u(t, \vec{\boldsymbol{x}}_q; \vec{\boldsymbol{x}}_s)u(t + \tau, \vec{\boldsymbol{x}}_{q'}; \vec{\boldsymbol{x}}_{s'})$ for $s' \neq s$ are included. In fact it is possible to analyze this modified imaging function in the same way as we have analyzed the imaging function $\mathcal{I}_{\mathrm{CC}}$ defined by (2.5). We find that the mean modified imaging is equal to the mean imaging function $\mathbb{E}[\mathcal{I}_{\mathrm{CC}}]$ described in Proposition 4.1, which shows that the resolution properties of the two imaging functions are identical. But the SNR of the modified imaging function is much lower than that of the imaging function $\mathcal{I}_{\mathrm{CC}}$,

$$\mathrm{SNR}_{\mathrm{CCmod}} = \mathrm{SNR}_{\mathrm{CC}} \frac{I_{\mathrm{s}}^{1/2}}{N_{\mathrm{s}}} < \mathrm{SNR}_{\mathrm{CC}},$$

where I_{s} is defined as in (6.2), which shows that it is always smaller than N_{s}^2. Note that if

$X_{\mathrm{cs}} \geq b$, then there is no source diversity at the surface, so $I_s \sim N_{\mathrm{s}}^2$ and both SNRs are equal and small, and hence the images are poor. When $X_{\mathrm{cs}} < b$ there is source diversity, but the method using the correlations (7.8) does not benefit from it by removing the crossed terms, which explains why its quality in terms of SNR is lower than that of $\mathcal{I}_{\mathrm{CC}}$ using the cross correlations (2.6). This confirms that the imaging function $\mathcal{I}_{\mathrm{CC}}$ is the correct way to image the reflector.

7.4. Comparison with coherent interferometric imaging. For completeness, we also plot images obtained with other imaging functions.

We consider first coherent interferometry (CINT), a method that was proposed and analyzed in [5] for imaging in weakly scattering media, in a regime where multiple scattering due to the inhomogeneities impedes the imaging process. In such media KM becomes statistically unstable, i.e., produces images that have random fluctuations (noise) which depend on the fluctuations of the velocity in the propagation medium. CINT consists of back-propagating cross correlations of the traces over appropriate space-frequency windows. It can be viewed as a smoothed Wigner process of the data [6] that is statistically stable in weakly scattering media [7]. The support of the windows in frequency is determined by the decoherence frequency Ω_d, while it is the decoherence length $X_d(\omega)$ that determines the support of the windows in space, i.e., in the receiver (or source) offset direction. These two decoherence parameters that depend on the data and affect the resolution of the method can be determined adaptively during the image formation using the approach proposed in [6]. CINT is a statistically stable method and has been proven to have much better SNR than KM in weakly scattering media [4]. In the imaging configuration considered here the medium between the array on the surface and the auxiliary array is a strongly scattering medium and CINT is not expected to improve the results. However, CINT should be used with virtual array imaging when the medium below the auxiliary array is weakly scattering.

We show in Figure 10 the image obtained using a CINT imaging function using the surface array data in which the cut-off parameters are optimized according to the method prescribed in [6]:

$$\mathcal{I}_{\mathrm{CINT}}(\vec{\boldsymbol{y}}^S) = \iint\limits_{|\omega-\omega'|\leq\Omega_d} d\omega d\omega' \sum_{\substack{s,s'=1 \\ |\vec{\boldsymbol{x}}_s-\vec{\boldsymbol{x}}_{s'}|\leq X_d(\frac{\omega+\omega'}{2})}}^{N_{\mathrm{s}}} \sum_{\substack{r,r'=1 \\ |\vec{\boldsymbol{x}}_r-\vec{\boldsymbol{x}}_{r'}|\leq X_d(\frac{\omega+\omega'}{2})}}^{N_{\mathrm{r}}} \hat{u}(\omega,\vec{\boldsymbol{x}}_r;\vec{\boldsymbol{x}}_s)\overline{\hat{u}(\omega',\vec{\boldsymbol{x}}_{r'};\vec{\boldsymbol{x}}_{s'})}$$

$$\times \exp\left\{-i\omega\left[\mathcal{T}(\vec{\boldsymbol{x}}_r,\vec{\boldsymbol{y}}^S)+\mathcal{T}(\vec{\boldsymbol{x}}_s,\vec{\boldsymbol{y}}^S)\right]+i\omega'\left[\mathcal{T}(\vec{\boldsymbol{x}}_{r'},\vec{\boldsymbol{y}}^S)+\mathcal{T}(\vec{\boldsymbol{x}}_{s'},\vec{\boldsymbol{y}}^S)\right]\right\}.$$

The optimal parameters are found to be $\Omega_d = B$ and $X_d(\omega) = \frac{32\lambda_0}{(\omega/\omega_0)}$, but the image is not yet good. Indeed, it is not expected that the CINT function gives a good image in this strongly scattering situation as proved and discussed in [4], for instance.

We show in Figure 11 the image obtained by the matched field imaging function using the data recorded on the surface array:

$$(7.9) \qquad \mathcal{I}_{\mathrm{MFr}}(\vec{\boldsymbol{y}}^S) = \int d\omega \left| \sum_{s=1}^{N_{\mathrm{s}}} \sum_{r=1}^{N_{\mathrm{r}}} \hat{u}(\omega,\vec{\boldsymbol{x}}_r;\vec{\boldsymbol{x}}_s)\exp\left\{-i\omega\left[\mathcal{T}(\vec{\boldsymbol{x}}_r,\vec{\boldsymbol{y}}^S)+\mathcal{T}(\vec{\boldsymbol{x}}_s,\vec{\boldsymbol{y}}^S)\right]\right\} \right|^2.$$
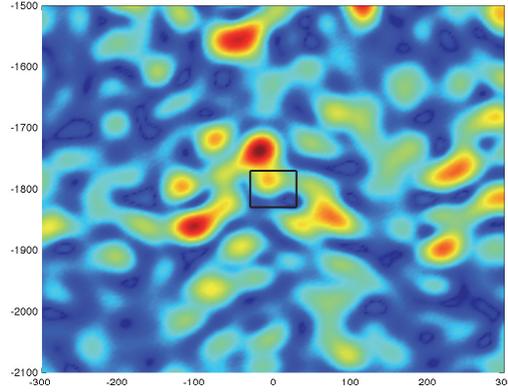
Figure 10. *Optimal CINT function using the data of the surface receiver array.*
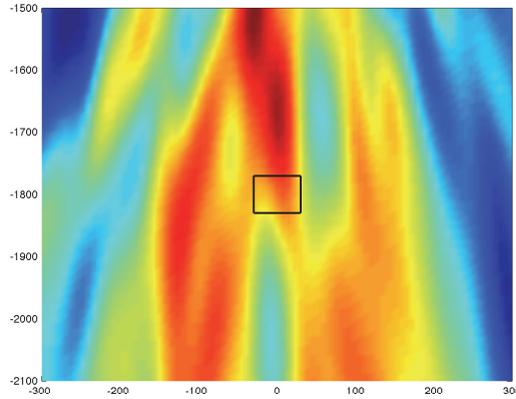
Figure 11. *MF image $\mathcal{I}_{\mathrm{MFr}}$ using the data of the surface receiver array.*

Note that it is a kind of CINT function with the special choice for the cut-off parameters $X_d = \infty$ and $\Omega_d = 0$. The image is definitely not good.

8. Signal to noise ratio computations. We consider in this section the two-dimensional imaging setup shown in Figure 3. We focus our attention on the SNR of the obtained image, and in particular we want to check whether there is good agreement between (6.6) and the numerical results. Note that the expressions in Propositions 4.1 and 6.1 are obtained in a three-dimensional context, and that in a two-dimensional context the theoretical SNR formula (6.6) now reads

$$(8.1) \qquad \mathrm{SNR}_{\mathrm{CC}} \approx \frac{\sigma_{\mathrm{ref}} X_{\mathrm{cq}}}{\lambda_0^2 (L_y - L)} \Big(\frac{b}{\max\{\Delta X_{\mathrm{s}}, X_{\mathrm{cs}}\}} \Big)^{1/2} \Big(\frac{a}{\max\{\Delta X_{\mathrm{q}}, X_{\mathrm{cq}}\}} \Big) \Big(\frac{B}{\omega_{\mathrm{c}}} \Big)^{1/2}.$$

We will therefore let vary the different parameters that appear in (8.1), i.e., the bandwidth, the number of sources $N_{\mathrm{s}} = b/\Delta X_{\mathrm{s}}$, the interdistance between sources ΔX_{s}, the number of receivers $N_{\mathrm{q}} = a/\Delta X_{\mathrm{q}}$, and the interdistance between receivers ΔX_{q}.

The SNR is computed numerically as follows. Let $\overline{\mathcal{I}^{\mathrm{D}}}(\vec{y})$ be the averaged absolute value of the image over a square of size $2\lambda_0 \times 2\lambda_0$ centered at $\vec{y}$. The SNR is computed as

$$(8.2) \qquad \mathrm{SNR} = \frac{\overline{\mathcal{I}^{\mathrm{D}}}(\vec{y}^*)}{\max_{\vec{y} \neq \vec{y}^*} \overline{\mathcal{I}^{\mathrm{D}}}(\vec{y})},$$

where $\vec{y}^*$ is the point at which the image admits its maximal value and $\vec{y} \neq \vec{y}^*$ means that squares of size $2\lambda_0 \times 2\lambda_0$ centered at $\vec{y}$ and $\vec{y}^*$ do not intersect.

8.1. Signal to noise ratio versus bandwidth. We apply here a treatment to the cross correlations in the Fourier domain in order to analyze the role of the bandwidth. More precisely, we apply a band-pass filter $H(f)$ to the recorded signals to retain only the frequency components centered at the central frequency $f_0 = 100\,\mathrm{Hz}$ with a bandwidth Δf: the filter has the form $H(f) = \mathbf{1}_{[f_0 - \Delta f/2, f_0 + \Delta f/2]}(|f|)$. The maximal value that Δf can take is 40Hz which corresponds to using the entire bandwidth of the pulse $F(t)$ (2.3).

We show in Figure 12 the $\mathcal{I}_{\mathrm{CC}}$ images obtained when the band-pass filter $H(f)$ is used with different values of Δf.

(a) $\Delta f = 40\,\mathrm{Hz}$.

(b) $\Delta f = 15\,\mathrm{Hz}$.

(c) $\Delta f = 10\,\mathrm{Hz}$.

(d) $\Delta f = 7.5\,\mathrm{Hz}$.
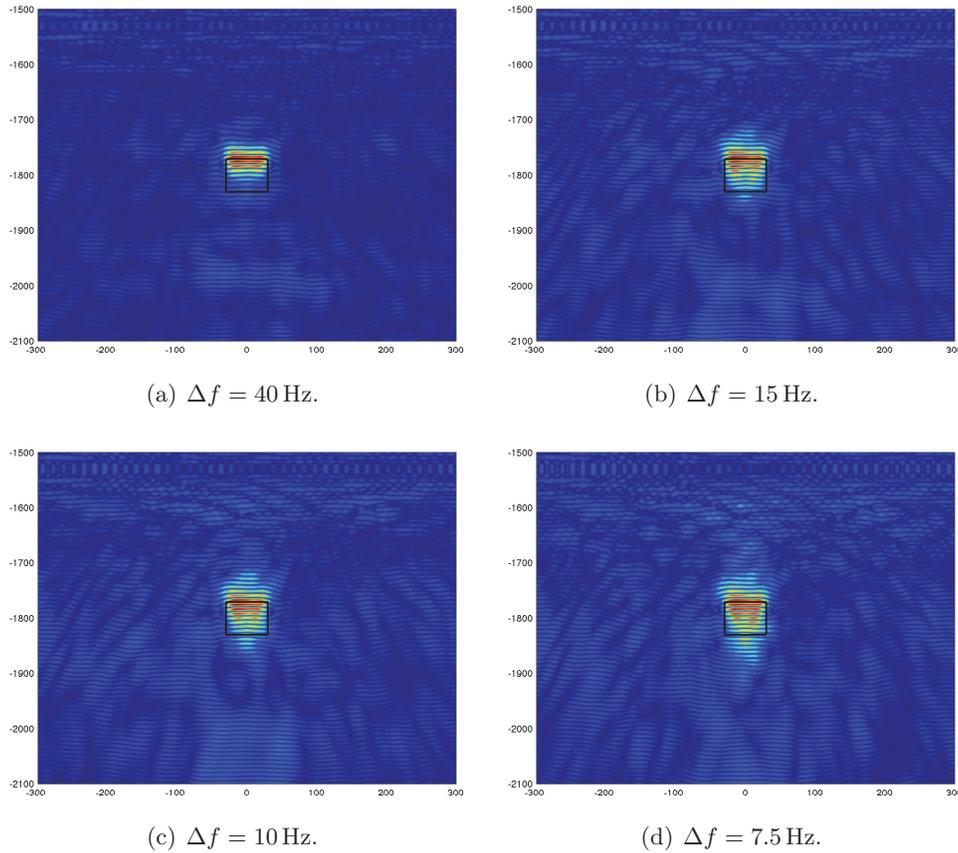
Figure 12. $\mathcal{I}_{\mathrm{CC}}$ for $N_{\mathrm{q}} = 61$ receivers with $\Delta X_{\mathrm{q}} = \lambda_0/2$ and $N_{\mathrm{s}} = 97$ sources with ΔX_{s}. We filter the data using the band-pass filter $H(f) = \mathbf{1}_{[f_0 - \Delta f/2, f_0 + \Delta f/2]}(|f|)$.

As predicted by the theory, bandwidth affects both the image resolution and the SNR. The range resolution is c_0/B, and therefore as the effective bandwidth (here Δf) decreases the image becomes less focused in range. Loss of resolution is also accompanied by loss in SNR, and we observe that the amplitude of the ghosts in the image increases as the bandwidth decreases.

Table 1

Δf (in Hz)	40	15	10	7.5
% of signal kept	100	65.81	53.14	45.98
SNR	23.93	10.16	6.13	3.48
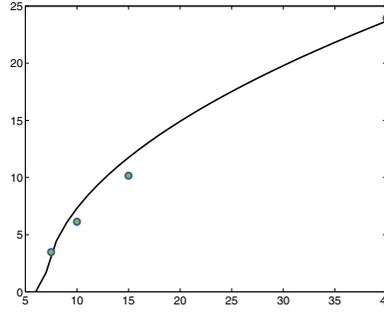
Figure 13. *Plot of measured SNR (blue dots) as a function of the bandwidth Δf and regression (black line).*

We plot in Figure 13 the value of the SNR (given in Table 1) with respect to the bandwidth Δf (blue circles) and the regression equation given by (8.3) (black line). SNR does linearly depend on the square root of the bandwidth as predicted by the theory (see Proposition 6.2 and relation (8.1)):

$$(8.3) \qquad \mathrm{SNR} = \sqrt{16.9\Delta f - 115.5}.$$

8.2. Signal to noise ratio versus number of sources. We computed the $\mathcal{I}_{\mathrm{CC}}$ images and their SNR for various values of the parameters N_s and ΔX_s. As an example, we show in Figure 14 imaging results for array apertures $b = (N_\mathrm{s} - 1)\Delta X_\mathrm{s} = 8\lambda_0, 18\lambda_0$, and $28\lambda_0$ (from left to right). These results suggest that SNR depends on the source array aperture. More precisely, SNR is linear with the square root of b as predicted by the theory (see Proposition 6.2 and relation (8.1)). This is illustrated in Figure 15 where we plot the value of the SNR with respect to b and the regression equation given by (8.4) (black line):

$$(8.4) \qquad \mathrm{SNR} = \sqrt{11.96\, b - 50.53}.$$

We also observe in Figure 14 that the source array aperture does not affect the resolution of the image as predicted by the theory (see Proposition 4.2).

8.3. Signal to noise ratio versus number of receivers. We computed the $\mathcal{I}_{\mathrm{CC}}$ images and their SNR for various values of the parameters N_q and ΔX_q. Recall that the theory (see Proposition 6.2 and relation (8.1)) suggests that SNR is linear with respect to the auxiliary

(a) $N_s = 17$, $\Delta X_s = \lambda_0/2$. (b) $N_s = 37$, $\Delta X_s = \lambda_0/2$. (c) $N_s = 57$, $\Delta X_s = \lambda_0/2$.

(d) $N_s = 9$, $\Delta X_s = \lambda_0$. (e) $N_s = 19$, $\Delta X_s = \lambda_0$. (f) $N_s = 29$, $\Delta X_s = \lambda_0$.
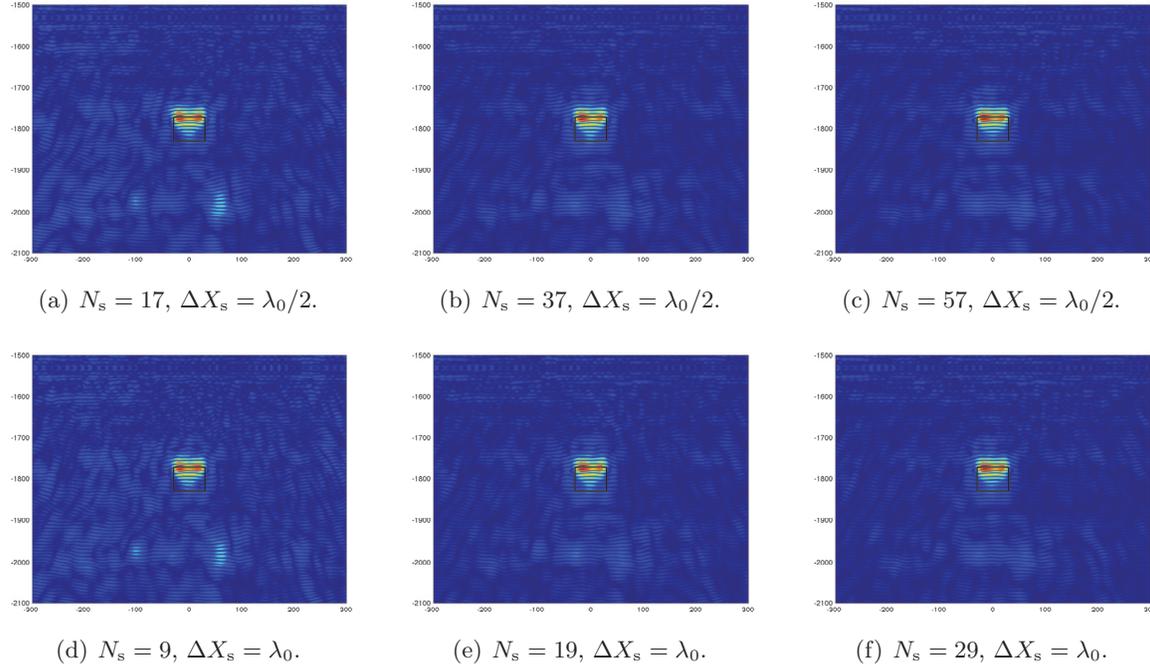
Figure 14. *Plot of $\mathcal{I}_{CC}$ for source array aperture $b = (N_s - 1)\Delta X_s = 8\lambda_0, 18\lambda_0$, and $28\lambda_0$ (from left to right). The number of receivers is $N_q = 61$ and the interdistance between receivers is $\Delta X_q = \lambda_0/2$.*
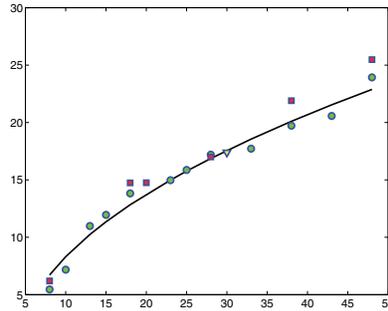
Figure 15. *Plot of measured SNR as a function of b and regression (black line). Blue circles correspond to $\Delta X_s = \lambda_0/2$, red squares correspond to $\Delta X_s = \lambda_0$, and the yellow triangle stands for $\Delta X_s = 3\lambda_0/2$.*

array aperture a as long as ΔX_q is smaller than X_{cq}. Otherwise SNR is linear with respect to $X_{cq}a/\Delta X_q$, which suggests that for a fixed array aperture, SNR increases as ΔX_q decreases. It is this latter behavior that we observe in our numerical results as illustrated in Figures 16–17. Indeed, in Figure 16 we plot the measured SNR as a function of $1/\Delta X_q$ for a fixed array aperture $a = 21\lambda_0$. We also plot the linear regression equation (black line),

$$(8.5) \qquad\qquad\qquad \text{SNR} = 421.2\frac{1}{\Delta X_q} - 5.76.$$

We observe that SNR is linear with respect to $1/\Delta X_q$ as predicted by relation (8.1).
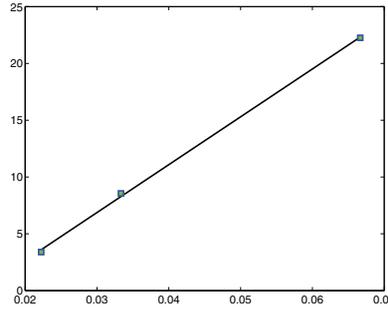
Figure 16. *Plot of measured SNR as a function of $1/\Delta X_{\mathrm{q}}$ for a fixed array aperture $a = 21\lambda_0$.*
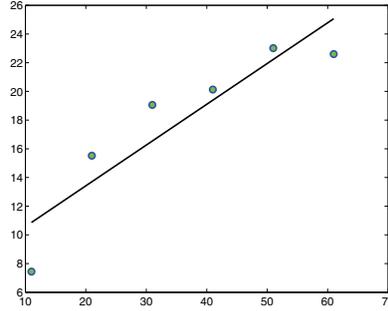
Figure 17. *Plot of measured SNR as a function of N_{q} (blue circles) and regression obtained for $\Delta X_{\mathrm{q}} = \lambda_0/2$ (black line).*

SNR is also linear with respect to N_{q} since for fixed ΔX_{q}, we have $X_{\mathrm{cq}}a/\Delta X_{\mathrm{q}} = X_{\mathrm{cq}}N_{\mathrm{q}}$. This is confirmed by our numerical simulations as can be seen in Figure 17, where we plot the measured SNR as a function of N_{q} for $\Delta X_{\mathrm{q}} = \lambda_0/2$. The linear regression in this case is

$$(8.6) \qquad\qquad \mathrm{SNR} = 0.284N_{\mathrm{q}} + 7.74.$$

9. Numerical results when the reflector is also in a randomly inhomogeneous medium. The geometry of the numerical setup is the same as in section 7 but the propagation medium is different. Here, the medium between the auxiliary array and the reflector is also inhomogeneous. It is either a layered or an isotropic random medium with small strength of fluctuations (σ is either 0.02 or 0.04).

The medium between the source and the auxiliary array is a strongly scattering medium constructed using (7.1) with $\sigma = 0.1$ in the region $(-25\lambda_0, 25\lambda_0) \times (-50\lambda_0, -5\lambda_0)$.

It can be seen that the migration of the cross correlation matrix of the auxiliary array data still gives good images in this weakly scattering situation. We also observe that the size of the receiver array a affects both the resolution and the SNR of the image. The cross-range resolution is $\lambda_0(L_y - L)/a$, and therefore as the array aperture increases, the image resolution in cross-range improves. Increasing the array aperture also benefits the SNR of the image as we see by the reduction of the amplitude of the ghosts in Figures 18 and 19 (compare the middle and right images of Figure 18 with those in Figure 19). As scattering increases in the medium between the auxiliary array and the reflector, we expect the images to become more
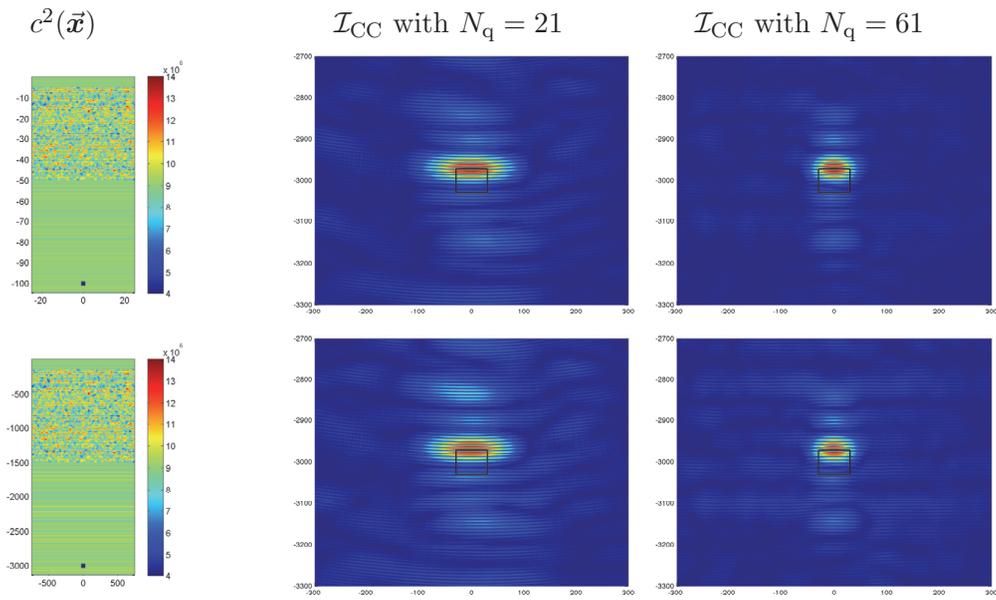
Figure 18. *Results obtained using cross correlations on the auxiliary receiver array. The medium above the auxiliary array is constructed using* (7.1) *with* $\sigma = 0.1$, *while the medium below the auxiliary array is a layered medium with* $\ell_x = \lambda_0/20$, $\sigma = 0.02$ *for the top row images and* $\ell_x = \lambda_0/20$, $\sigma = 0.04$ *for the bottom row images.*
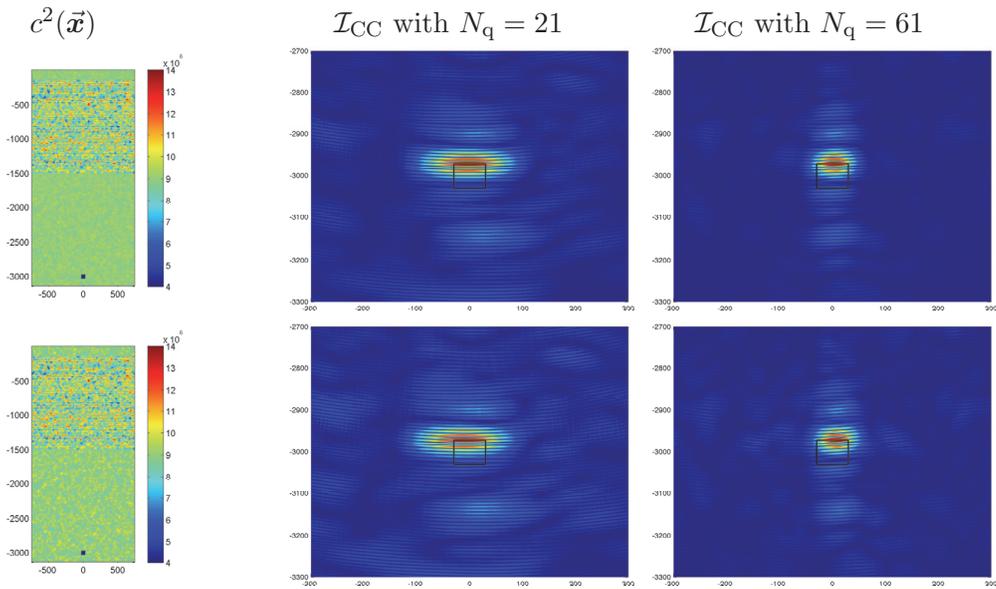
Figure 19. *Results obtained using cross correlations on the auxiliary receiver array. The medium above the auxiliary array is the same as in Figure* 18, *while the medium below the auxiliary array is now an isotropic medium with* $\ell_x = \lambda_0/2$, $\sigma = 0.02$ *for the top row images and* $\ell_x = \lambda_0/2$, $\sigma = 0.04$ *for the bottom row images.*

noisy and lose statistical stability. It is then anticipated that CINT techniques could be used to improve the stability of the image as was done with active array data [5, 6].

10. Conclusion. In this paper we have analyzed an imaging configuration as in Figure 1 in which the data of an auxiliary receiver array are available to image a reflector embedded below a strongly scattering medium. The overall conclusion is that migration of the cross correlation matrix of the auxiliary array data gives a much better image than the migration of the data themselves. This is observed when comparing Figures 5 and 8 obtained by using two-dimensional full wave simulated data. The same conclusion was drawn from the theoretical analysis carried out in sections 4 and 6 using the Kronecker model for the incoherent field transmitted through the scattering medium. The Kronecker model is simple and allows us to analyze in an explicit way the resolution and the stability properties of the imaging function. Moreover, its predictions are in full agreement with not only the results of the numerical simulations but also with the theoretical predictions obtained from the analysis of some asymptotic regimes, in particular the random paraxial regime (see section 5 and [19]).

Appendix A. Proof of Proposition 4.1. In this appendix we give the proof of Proposition 4.1. From the definition (2.5) the mean imaging function has the form

$$\mathbb{E}\big[\mathcal{I}_{\mathrm{CC}}(\vec{\boldsymbol{y}}^S)\big] = \sum_{s=1}^{N_{\mathrm{s}}} \sum_{q,q'=1}^{N_{\mathrm{q}}} \int \mathbb{E}\big[\overline{\hat{u}(\omega,\vec{\boldsymbol{x}}_q;\vec{\boldsymbol{x}}_s)}\hat{u}(\omega,\vec{\boldsymbol{x}}_{q'};\vec{\boldsymbol{x}}_s)\big]$$
$$\times \exp\Big(-i\omega\frac{|\vec{\boldsymbol{x}}_q-\vec{\boldsymbol{y}}^S|+|\vec{\boldsymbol{x}}_{q'}-\vec{\boldsymbol{y}}^S|}{c_0}\Big)d\omega.$$

The recorded field $\hat{u}$ has the form (3.3) so that the mean imaging function is the sum of three main contributions:

$$\mathbb{E}\big[\mathcal{I}_{\mathrm{CC}}(\vec{\boldsymbol{y}}^S)\big]_I = \sum_{s=1}^{N_{\mathrm{s}}} \sum_{q,q'=1}^{N_{\mathrm{q}}} \int \mathbb{E}\big[\overline{\hat{u}_0(\omega,\vec{\boldsymbol{x}}_q;\vec{\boldsymbol{x}}_s)}\hat{u}_0(\omega,\vec{\boldsymbol{x}}_{q'};\vec{\boldsymbol{x}}_s)\big]$$
$$\times \exp\Big(-i\omega\frac{|\vec{\boldsymbol{x}}_q-\vec{\boldsymbol{y}}^S|+|\vec{\boldsymbol{x}}_{q'}-\vec{\boldsymbol{y}}^S|}{c_0}\Big)d\omega,$$

$$\mathbb{E}\big[\mathcal{I}_{\mathrm{CC}}(\vec{\boldsymbol{y}}^S)\big]_{II} = -2i\frac{\sigma_{\mathrm{ref}}}{c_0^3} \sum_{s=1}^{N_{\mathrm{s}}} \sum_{q,q'=1}^{N_{\mathrm{q}}} \int \omega^3 \int_{\mathbb{R}^2} \mathbb{E}\big[\overline{\hat{u}_0(\omega,\vec{\boldsymbol{x}}_q;\vec{\boldsymbol{x}}_s)}\hat{u}_0(\omega,(\boldsymbol{x},-L);\vec{\boldsymbol{x}}_s)\big]$$
$$\times \hat{G}_0(\omega,\vec{\boldsymbol{x}}_{q'};\vec{\boldsymbol{y}})\hat{G}_0(\omega,\vec{\boldsymbol{y}};(\boldsymbol{x},-L)) \exp\Big(-i\omega\frac{|\vec{\boldsymbol{x}}_q-\vec{\boldsymbol{y}}^S|+|\vec{\boldsymbol{x}}_{q'}-\vec{\boldsymbol{y}}^S|}{c_0}\Big)d\boldsymbol{x}d\omega,$$

$$\mathbb{E}\big[\mathcal{I}_{\mathrm{CC}}(\vec{\boldsymbol{y}}^S)\big]_{III} = 2i\frac{\sigma_{\mathrm{ref}}}{c_0^3} \sum_{s=1}^{N_{\mathrm{s}}} \sum_{q,q'=1}^{N_{\mathrm{q}}} \int \omega^3 \int_{\mathbb{R}^2} \mathbb{E}\big[\overline{\hat{u}_0(\omega,(\boldsymbol{x},-L);\vec{\boldsymbol{x}}_s)}\hat{u}_0(\omega,\vec{\boldsymbol{x}}_{q'};\vec{\boldsymbol{x}}_s)\big]$$
$$\times \overline{\hat{G}_0(\omega,\vec{\boldsymbol{x}}_q;\vec{\boldsymbol{y}})\hat{G}_0(\omega,\vec{\boldsymbol{y}};(\boldsymbol{x},-L))} \exp\Big(-i\omega\frac{|\vec{\boldsymbol{x}}_q-\vec{\boldsymbol{y}}^S|+|\vec{\boldsymbol{x}}_{q'}-\vec{\boldsymbol{y}}^S|}{c_0}\Big)d\boldsymbol{x}d\omega.$$

There is also a fourth contribution of order σ_{ref}^2 that is neglected consistently with the Born approximation.

Using the form (3.2) of the covariance of the illumination field $\hat{u}_0$, the first contribution is

$$\mathbb{E}\big[\mathcal{I}_{\mathrm{CC}}(\vec{\boldsymbol{y}}^S)\big]_I = N_{\mathrm{s}} \sum_{q,q'=1}^{N_{\mathrm{q}}} \exp\Big(-\frac{|\boldsymbol{x}_q - \boldsymbol{x}_{q'}|^2}{X_{\mathrm{cq}}^2}\Big)$$
$$\times \int |\hat{F}(\omega)|^2 \exp\Big(-i\omega\frac{|\vec{\boldsymbol{x}}_q - \vec{\boldsymbol{y}}^S| + |\vec{\boldsymbol{x}}_{q'} - \vec{\boldsymbol{y}}^S|}{c_0}\Big)d\omega.$$

The pulse width $1/B$ of the source is much smaller than the travel time $(L_y - L)/c_0$ from the auxiliary receiver array to the reflector. Consequently the integral in the first contribution is vanishing.

Using (3.2), the second contribution is

$$\mathbb{E}\big[\mathcal{I}_{\mathrm{CC}}(\vec{\boldsymbol{y}}^S)\big]_{II} = -2i\frac{N_{\mathrm{s}}\sigma_{\mathrm{ref}}}{c_0^3} \sum_{q,q'=1}^{N_{\mathrm{q}}} \int \int_{\mathbb{R}^2} \omega^3 |\hat{F}(\omega)|^2 \exp\Big(-\frac{|\boldsymbol{x} - \boldsymbol{x}_q|^2}{X_{\mathrm{cq}}^2}\Big)$$
$$\times \hat{G}_0(\omega, \vec{\boldsymbol{x}}_{q'}; \vec{\boldsymbol{y}}) \hat{G}_0(\omega, \vec{\boldsymbol{y}}; (\boldsymbol{x}, -L)) \exp\Big(-i\omega\frac{|\vec{\boldsymbol{x}}_q - \vec{\boldsymbol{y}}^S| + |\vec{\boldsymbol{x}}_{q'} - \vec{\boldsymbol{y}}^S|}{c_0}\Big)d\boldsymbol{x}d\omega.$$

Using the explicit form of the homogeneous Green's function (3.4) and the paraxial approximation $a \ll L_y - L$, the amplitude factors of the two homogeneous Green's functions can be considered as constant and

$$\mathbb{E}\big[\mathcal{I}_{\mathrm{CC}}(\vec{\boldsymbol{y}}^S)\big]_{II} = -i\frac{N_{\mathrm{s}}\sigma_{\mathrm{ref}}}{8\pi^2 c_0^3 (L_y - L)^2} \sum_{q,q'=1}^{N_{\mathrm{q}}} \int \int_{\mathbb{R}^2} \omega^3 |\hat{F}(\omega)|^2$$
$$\times \exp\Big(-\frac{|\boldsymbol{x} - \boldsymbol{x}_q|^2}{X_{\mathrm{cq}}^2} + i\frac{\omega}{c_0}D\big((\boldsymbol{x}, -L), \vec{\boldsymbol{x}}_q, \vec{\boldsymbol{x}}_{q'}\big)\Big)d\boldsymbol{x}d\omega,$$
$$D\big(\vec{\boldsymbol{x}}, \vec{\boldsymbol{x}}_q, \vec{\boldsymbol{x}}_{q'}\big) = |\vec{\boldsymbol{x}} - \vec{\boldsymbol{y}}| + |\vec{\boldsymbol{x}}_{q'} - \vec{\boldsymbol{y}}| - |\vec{\boldsymbol{x}}_q - \vec{\boldsymbol{y}}^S| - |\vec{\boldsymbol{x}}_{q'} - \vec{\boldsymbol{y}}^S|.$$

Parameterizing the search point as $\vec{\boldsymbol{y}}^S = (\boldsymbol{y} + \boldsymbol{\xi}, -L_y - \eta)$ and using again the paraxial approximation, the term D can be expanded as (for $\vec{\boldsymbol{x}} = (\boldsymbol{x}, -L)$)

$$D\big(\vec{\boldsymbol{x}}, \vec{\boldsymbol{x}}_q, \vec{\boldsymbol{x}}_{q'}\big) = -2\eta + \frac{1}{(L_y - L)}\Big((\boldsymbol{x} - \boldsymbol{x}_q)\cdot\Big(\frac{\boldsymbol{x}_q + \boldsymbol{x}}{2} - \boldsymbol{y}\Big) + \boldsymbol{\xi}\cdot(\boldsymbol{x}_{q'} - \boldsymbol{y}) + \boldsymbol{\xi}\cdot(\boldsymbol{x}_q - \boldsymbol{y})\Big).$$

Substituting and integrating in $\boldsymbol{x}$ gives

$$\mathbb{E}\big[\mathcal{I}_{\mathrm{CC}}(\vec{\boldsymbol{y}}^S)\big]_{II} = -i\frac{N_{\mathrm{s}}\sigma_{\mathrm{ref}}X_{\mathrm{cq}}^2}{8c_0^3\pi(L_y - L)^2} \sum_{q,q'=1}^{N_{\mathrm{q}}} \int \omega^3 |\hat{F}(\omega)|^2 \exp\Big(i\frac{\omega}{c_0}\Big(-2\eta + \frac{\boldsymbol{\xi}\cdot(\boldsymbol{x}_{q'} - \boldsymbol{y})}{L_y - L}\Big)\Big)$$
$$\times \exp\Big(i\frac{\omega}{c_0}\frac{\boldsymbol{\xi}\cdot(\boldsymbol{x}_q - \boldsymbol{y})}{L_y - L} - \frac{\omega^2 X_{\mathrm{cq}}^2}{4c_0^2(L_y - L)^2}|\boldsymbol{x}_q - \boldsymbol{y}|^2\Big)d\omega.$$

The hypothesis $\Delta X_{\mathrm{q}} \ll \lambda_0(L_y - L)/a$ allows us to substitute a continuous integral for the discrete sum in q, q' and to get the desired result.

The third contribution can be addressed in the same way, but it gives no contribution because the phases of the cross correlation term and of the product of homogeneous Green's functions do not compensate each other.

Appendix B. Proof of Proposition 6.1. In this appendix we give the proof of Proposition 6.1. The variance of $\mathcal{I}_{\mathrm{CC}}(\vec{\boldsymbol{y}}^S)$ is dominated by contribution of the illumination field $\hat{u}_0$:

$$
\mathbb{E}\big[\mathcal{I}_{\mathrm{CC}}(\vec{\boldsymbol{y}}^S)^2\big] = \sum_{s,s'=1}^{N_{\mathrm{s}}} \sum_{q,q',\tilde{q},\tilde{q}'=1}^{N_{\mathrm{q}}} \iint d\omega d\omega'
$$
$$
\mathbb{E}\big[\hat{u}_0(\omega,\vec{\boldsymbol{x}}_q;\vec{\boldsymbol{x}}_s)\overline{\hat{u}_0(\omega,\vec{\boldsymbol{x}}_{\tilde{q}};\vec{\boldsymbol{x}}_s)}\hat{u}_0(\omega',\vec{\boldsymbol{x}}_{q'};\vec{\boldsymbol{x}}_{s'})\hat{u}_0(\omega',\vec{\boldsymbol{x}}_{\tilde{q}'};\vec{\boldsymbol{x}}_{s'})\big]
$$
$$
\times \exp\Big(-i\frac{\omega}{c_0}[|\vec{\boldsymbol{y}}^S - \vec{\boldsymbol{x}}_q| + |\vec{\boldsymbol{y}}^S - \vec{\boldsymbol{x}}_{\tilde{q}}|] + i\frac{\omega'}{c_0}[|\vec{\boldsymbol{y}}^S - \vec{\boldsymbol{x}}_{q'}| + |\vec{\boldsymbol{y}}^S - \vec{\boldsymbol{x}}_{\tilde{q}'}|]\Big).
$$

The fourth-order moment of a complex Gaussian vector (Z_1, Z_2, Z_3, Z_4) can be expressed in terms of the second-order moments by the Gaussian summation rule:

$$
\mathbb{E}[Z_1 Z_2 Z_3 Z_4] = \mathbb{E}[Z_1 Z_2]\mathbb{E}[Z_3 Z_4] + \mathbb{E}[Z_1 Z_3]\mathbb{E}[Z_2 Z_4] + \mathbb{E}[Z_1 Z_4]\mathbb{E}[Z_2 Z_3].
$$

Using the Gaussian property of the field $\hat{u}_0$, the second moment of $\mathcal{I}_{\mathrm{CC}}(\vec{\boldsymbol{y}}^S)$ consists of the sum of three terms:

$$
\mathbb{E}\big[\mathcal{I}_{\mathrm{CC}}(\vec{\boldsymbol{y}}^S)^2\big] = \sum_{s,s'=1}^{N_{\mathrm{s}}} \sum_{q,q',\tilde{q},\tilde{q}'=1}^{N_{\mathrm{q}}} \iint d\omega d\omega'
$$
$$
\Big[\mathbb{E}[\hat{u}_0(\omega,\vec{\boldsymbol{x}}_q;\vec{\boldsymbol{x}}_s)\overline{\hat{u}_0(\omega,\vec{\boldsymbol{x}}_{\tilde{q}};\vec{\boldsymbol{x}}_s)}]\mathbb{E}[\overline{\hat{u}_0(\omega',\vec{\boldsymbol{x}}_{q'};\vec{\boldsymbol{x}}_{s'})}\hat{u}_0(\omega',\vec{\boldsymbol{x}}_{\tilde{q}'};\vec{\boldsymbol{x}}_{s'})]
$$
$$
+ \mathbb{E}[\hat{u}_0(\omega,\vec{\boldsymbol{x}}_q;\vec{\boldsymbol{x}}_s)\overline{\hat{u}_0(\omega',\vec{\boldsymbol{x}}_{q'};\vec{\boldsymbol{x}}_{s'})}]\mathbb{E}[\overline{\hat{u}_0(\omega,\vec{\boldsymbol{x}}_{\tilde{q}};\vec{\boldsymbol{x}}_s)}\hat{u}_0(\omega',\vec{\boldsymbol{x}}_{\tilde{q}'};\vec{\boldsymbol{x}}_{s'})]
$$
$$
+ \mathbb{E}[\hat{u}_0(\omega,\vec{\boldsymbol{x}}_q;\vec{\boldsymbol{x}}_s)\hat{u}_0(\omega',\vec{\boldsymbol{x}}_{\tilde{q}'};\vec{\boldsymbol{x}}_{s'})]\mathbb{E}[\overline{\hat{u}_0(\omega,\vec{\boldsymbol{x}}_{\tilde{q}};\vec{\boldsymbol{x}}_s)}\overline{\hat{u}_0(\omega',\vec{\boldsymbol{x}}_{q'};\vec{\boldsymbol{x}}_{s'})}]\Big]
$$
$$
\times \exp\Big(-i\frac{\omega}{c_0}[|\vec{\boldsymbol{y}}^S - \vec{\boldsymbol{x}}_q| + |\vec{\boldsymbol{y}}^S - \vec{\boldsymbol{x}}_{\tilde{q}}|] + i\frac{\omega'}{c_0}[|\vec{\boldsymbol{y}}^S - \vec{\boldsymbol{x}}_{q'}| + |\vec{\boldsymbol{y}}^S - \vec{\boldsymbol{x}}_{\tilde{q}'}|]\Big).
$$

Using the form (3.2) of the covariance function of the illumination field, the first term is

$$
\mathbb{E}\big[\mathcal{I}_{\mathrm{CC}}(\vec{\boldsymbol{y}}^S)^2\big]_I = \Big| N_{\mathrm{s}} \sum_{q,\tilde{q}=1}^{N_{\mathrm{q}}} \exp\Big(-\frac{|\boldsymbol{x}_q - \boldsymbol{x}_{\tilde{q}}|^2}{X_{\mathrm{cq}}^2}\Big)
$$
$$
\times \int d\omega |\hat{F}(\omega)|^2 \exp\Big(-i\frac{\omega}{c_0}[|\vec{\boldsymbol{y}}^S - \vec{\boldsymbol{x}}_q| + |\vec{\boldsymbol{y}}^S - \vec{\boldsymbol{x}}_{\tilde{q}}|]\Big) \Big|^2.
$$

This term is in fact $\mathbb{E}\big[\mathcal{I}_{\mathrm{CC}}(\vec{\boldsymbol{y}}^S)\big]_I^2$ (cf. Appendix A) and it is vanishing because the sum of travel times is much larger than the pulse width of the source.

Using (3.2) again and the expansion

$$
|\vec{\boldsymbol{y}}^S - \vec{\boldsymbol{x}}_q| - |\vec{\boldsymbol{y}}^S - \vec{\boldsymbol{x}}_{q'}| = \frac{1}{(L_y - L)}\Big(\frac{\boldsymbol{x}_q + \boldsymbol{x}_{q'}}{2} - \boldsymbol{y}^S\Big) \cdot (\boldsymbol{x}_q - \boldsymbol{x}_{q'}),
$$

the second term in the expression of $\mathbb{E}\big[\mathcal{I}_{\mathrm{CC}}(\vec{y}^S)^2\big]$ is

$$
\mathbb{E}\big[\mathcal{I}_{\mathrm{CC}}(\vec{y}^S)^2\big]_{II} = \sum_{s,s'=1}^{N_{\mathrm{s}}} \sum_{q,q',\tilde{q},\tilde{q}'=1}^{N_{\mathrm{q}}} \left[\iint |\hat{F}(\omega)|^2 |\hat{F}(\omega')|^2 \exp\Big(-\frac{2(\omega-\omega')^2}{\omega_c^2} \Big) d\omega d\omega' \right]
$$

$$
\times \exp\Big(-\frac{|\boldsymbol{x}_q - \boldsymbol{x}_{q'}|^2}{X_{\mathrm{cq}}^2} - \frac{|\boldsymbol{x}_{\tilde{q}} - \boldsymbol{x}_{\tilde{q}'}|^2}{X_{\mathrm{cq}}^2} - 2\frac{|\boldsymbol{x}_s - \boldsymbol{x}_{s'}|^2}{X_{\mathrm{cs}}^2} \Big)
$$

$$
\times \exp\Big(-i\frac{\omega_0}{c_0(L_y-L)} \Big(\frac{\boldsymbol{x}_q + \boldsymbol{x}_{q'}}{2} - \boldsymbol{y}^S \Big) \cdot (\boldsymbol{x}_q - \boldsymbol{x}_{q'}) \Big)
$$

$$
\times \exp\Big(-i\frac{\omega_0}{c_0(L_y-L)} \Big(\frac{\boldsymbol{x}_{\tilde{q}} + \boldsymbol{x}_{\tilde{q}'}}{2} - \boldsymbol{y}^S \Big) \cdot (\boldsymbol{x}_{\tilde{q}} - \boldsymbol{x}_{\tilde{q}'}) \Big).
$$

The hypothesis $\omega_c \ll B$ gives

$$
\iint |\hat{F}(\omega)|^2 |\hat{F}(\omega')|^2 \exp\Big(-\frac{2(\omega-\omega')^2}{\omega_c^2} \Big) d\omega d\omega'
$$

$$
= \iint \Big| \hat{F}\Big(\omega + \frac{h}{2}\Big) \Big|^2 \Big| \hat{F}\Big(\omega - \frac{h}{2}\Big) \Big|^2 \exp\Big(-\frac{2h^2}{\omega_c^2} \Big) dh d\omega
$$

$$
\overset{\omega_c \ll B}{=} \frac{\sqrt{\pi}}{\sqrt{2}} \omega_c \int |\hat{F}(\omega)|^4 d\omega.
$$

Using this relation and the definition (6.2) of I_{s}, the expression of $\mathbb{E}\big[\mathcal{I}_{\mathrm{CC}}(\vec{y}^S)^2\big]_{II}$ can be simplified into

$$
\mathbb{E}\big[\mathcal{I}_{\mathrm{CC}}(\vec{y}^S)^2\big]_{II} = \frac{\sqrt{\pi}}{\sqrt{2}} \omega_c I_{\mathrm{s}} \left[\int |\hat{F}(\omega)|^4 d\omega \right]
$$

$$
\times \left[\sum_{q,q'=1}^{N_{\mathrm{q}}} \exp\Big(-\frac{|\boldsymbol{x}_q - \boldsymbol{x}_{q'}|^2}{X_{\mathrm{cq}}^2} - i\frac{\omega_0}{c_0(L_y-L)} \Big(\frac{\boldsymbol{x}_q + \boldsymbol{x}_{q'}}{2} - \boldsymbol{y}^S \Big) \cdot (\boldsymbol{x}_q - \boldsymbol{x}_{q'}) \Big) \right]^2.
$$

If $\Delta X_{\mathrm{q}} \gg X_{\mathrm{cq}}$, then only the terms $q = q'$ survive in the double sum:

(B.1)
$$
\mathbb{E}\big[\mathcal{I}_{\mathrm{CC}}(\vec{y}^S)^2\big]_{II} = \frac{\sqrt{\pi}}{\sqrt{2}} \omega_c I_{\mathrm{s}} N_{\mathrm{q}}^2 \left[\int |\hat{F}(\omega)|^4 d\omega \right].
$$

If $\Delta X_{\mathrm{q}} \ll X_{\mathrm{cq}}$, then we can use the continuum approximation

$$
\sum_{q,q'=1}^{N_{\mathrm{q}}} \exp\Big(-\frac{|\boldsymbol{x}_q - \boldsymbol{x}_{q'}|^2}{X_{\mathrm{cq}}^2} - i\frac{\omega_0}{c_0(L_y-L)} \Big(\frac{\boldsymbol{x}_q + \boldsymbol{x}_{q'}}{2} - \boldsymbol{y}^S \Big) \cdot (\boldsymbol{x}_q - \boldsymbol{x}_{q'}) \Big)
$$

$$
= \sum_{q,q'=1}^{N_{\mathrm{q}}} \exp\Big(-\frac{|\boldsymbol{x}_q - \boldsymbol{x}_{q'}|^2}{X_{\mathrm{cq}}^2} - i\frac{\omega_0}{c_0(L_y-L)} \Big(\boldsymbol{x}_q + \frac{\boldsymbol{x}_{q'} - \boldsymbol{x}_q}{2} - \boldsymbol{y}^S \Big) \cdot (\boldsymbol{x}_q - \boldsymbol{x}_{q'}) \Big)
$$

$$
= \frac{N_{\mathrm{q}}}{a^2} \sum_{q=1}^{N_{\mathrm{q}}} \int_{[-a/2,a/2]^2 - \boldsymbol{x}_q} \exp\Big(-\frac{|\boldsymbol{x}|^2}{X_{\mathrm{cq}}^2} - i\frac{\omega_0}{c_0(L_y-L)} \Big(\boldsymbol{x}_q - \frac{\boldsymbol{x}}{2} - \boldsymbol{y}^S \Big) \cdot \boldsymbol{x} \Big) d\boldsymbol{x}.
$$

By using the fact that $X_{cq} \ll a$, the integral can be computed:

$$\sum_{q,q'=1}^{N_q} \exp\Big(-\frac{|\boldsymbol{x}_q - \boldsymbol{x}_{q'}|^2}{X_{cq}^2} - i\frac{\omega_0}{c_0(L_y - L)}\Big(\frac{\boldsymbol{x}_q + \boldsymbol{x}_{q'}}{2} - \boldsymbol{y}^S\Big)\cdot(\boldsymbol{x}_q - \boldsymbol{x}_{q'})\Big)$$

$$= \frac{N_q}{a^2}\sum_{q=1}^{N_q}\int_{\mathbb{R}^2}\exp\Big(-\frac{|\boldsymbol{x}|^2}{X_{cq}^2} - i\frac{\omega_0}{c_0(L_y - L)}\Big(\boldsymbol{x}_q - \frac{\boldsymbol{x}}{2} - \boldsymbol{y}^S\Big)\cdot\boldsymbol{x}\Big)d\boldsymbol{x},$$

$$(B.2)\qquad = \frac{N_q}{a^2}\sum_{q=1}^{N_q}\frac{\pi}{\frac{1}{X_{cq}^2} - \frac{i\omega_0}{2c_0(L_y - L)}}\exp\Big(-\frac{\frac{\omega_0^2}{4c_0^2(L_y-L)^2}|\boldsymbol{x}_q - \boldsymbol{y}^S|^2}{\frac{1}{X_{cq}^2} - \frac{i\omega_0}{2c_0(L_y - L)}}\Big).$$

If, additionally, $X_{cq} \ll \lambda_0(L_y - L)/a$, then we also have $X_{cq}^2 \ll \lambda_0(L_y - L)$ (because $X_{cq} \ll a$), so that

$$\sum_{q,q'=1}^{N_q}\exp\Big(-\frac{|\boldsymbol{x}_q - \boldsymbol{x}_{q'}|^2}{X_{cq}^2} - i\frac{\omega_0}{c_0(L_y - L)}\Big(\frac{\boldsymbol{x}_q + \boldsymbol{x}_{q'}}{2} - \boldsymbol{y}^S\Big)\cdot(\boldsymbol{x}_q - \boldsymbol{x}_{q'})\Big)$$

$$= \frac{N_q}{a^2}\sum_{q=1}^{N_q}\pi X_{cq}^2\exp\Big(-\frac{\omega_0^2 X_{cq}^2}{4c_0^2(L_y - L)^2}|\boldsymbol{x}_q - \boldsymbol{y}^S|^2\Big),$$

and the exponential terms in the sum are approximately equal to one, so that

$$(B.3)\qquad \mathbb{E}\big[\mathcal{I}_{CC}(\vec{\boldsymbol{y}}^S)^2\big]_{II} = \frac{I_s N_q^4}{a^4}\frac{\pi^{5/2}\omega_c X_{cq}^4}{2^{1/2}}\Big[\int |\hat{F}(\omega)|^4 d\omega\Big].$$

Otherwise, i.e., if $X_{cq} \gg \lambda_0(L_y - L)/a$, we can use the continuum approximation to compute the sum in (B.2):

$$\sum_{q,q'=1}^{N_q}\exp\Big(-\frac{|\boldsymbol{x}_q - \boldsymbol{x}_{q'}|^2}{X_{cq}^2} - i\frac{\omega_0}{c_0(L_y - L)}\Big(\frac{\boldsymbol{x}_q + \boldsymbol{x}_{q'}}{2} - \boldsymbol{y}^S\Big)\cdot(\boldsymbol{x}_q - \boldsymbol{x}_{q'})\Big)$$

$$= \frac{N_q^2}{a^4}\frac{\pi}{\frac{1}{X_{cq}^2} - \frac{i\omega_0}{2c_0(L_y - L)}}\int_{\mathbb{R}^2}\exp\Big(-\frac{\frac{\omega_0^2}{4c_0^2(L_y-L)^2}|\boldsymbol{x}|^2}{\frac{1}{X_{cq}^2} - \frac{i\omega_0}{2c_0(L_y - L)}}\Big)d\boldsymbol{x}$$

$$= \frac{N_q^2}{a^4}\frac{4\pi^2 c_0^2(L_y - L)^2}{\omega_0^2},$$

which gives

$$(B.4)\qquad \mathbb{E}\big[\mathcal{I}_{CC}(\vec{\boldsymbol{y}}^S)^2\big]_{II} = \frac{I_s N_q^4}{a^8}\frac{8\sqrt{2}\pi^{9/2}\omega_c c_0^4(L_y - L)^4}{\omega_0^4}\Big[\int |\hat{F}(\omega)|^4 d\omega\Big].$$

The third term in the expression of $\mathbb{E}\big[\mathcal{I}_{CC}(\vec{\boldsymbol{y}}^S)^2\big]$ can be analyzed in the same way but it does not give any contribution because it is proportional to

$$\int |\hat{F}(\omega)|^4\exp\Big(-4i\frac{\omega}{c_0}(L_y - L)\Big)d\omega,$$

and this is vanishing since the sum of travel times is much larger than the source pulse width.

Appendix C. Proof of Proposition 6.2. Let us assume that the Fourier transform of the source pulse profile has the normalized form

$$\hat{F}(\omega) = \hat{F}_0\Big(\frac{|\omega| - \omega_0}{B}\Big),$$

where ω_0 is the central frequency and B is the bandwidth. Here $\hat{F}_0$ is a normalized function that is supported in $[-1/2, 1/2]$.

If we do not write the multiplicative constants (such as 2π and quantities related to $\hat{F}_0$), we have by Proposition 4.2

$$|\mathbb{E}[\mathcal{I}_{\mathrm{CC}}(\vec{y})]| \approx \begin{cases} \dfrac{N_{\mathrm{s}}N_{\mathrm{q}}^2 B \sigma_{\mathrm{ref}}}{\lambda_0} \dfrac{X_{\mathrm{cq}}^2}{(L_y - L)^2 \lambda_0^2} & \text{if } X_{\mathrm{cq}} \ll \dfrac{\lambda_0(L_y - L)}{a}, \\[3mm] \dfrac{N_{\mathrm{s}}N_{\mathrm{q}}^2 B \sigma_{\mathrm{ref}}}{\lambda_0} \dfrac{1}{a^2} & \text{if } X_{\mathrm{cq}} \gg \dfrac{\lambda_0(L_y - L)}{a}, \end{cases}$$

and by Proposition 6.1

$$\mathrm{Var}\big(\mathcal{I}_{\mathrm{CC}}(\vec{y}^S)\big) \approx \begin{cases} I_{\mathrm{s}}N_{\mathrm{q}}^2 \omega_c B & \text{if } X_{\mathrm{cq}} \ll \Delta X_{\mathrm{q}}, \\[2mm] I_{\mathrm{s}}N_{\mathrm{q}}^4 \omega_c B \dfrac{X_{\mathrm{cq}}^4}{a^4} & \text{if } \Delta X_{\mathrm{q}} \ll X_{\mathrm{cq}} \ll \dfrac{\lambda_0(L_y - L)}{a}, \\[3mm] I_{\mathrm{s}}N_{\mathrm{q}}^4 \omega_c B \dfrac{(L_y - L)^4 \lambda_0^4}{a^8} & \text{if } X_{\mathrm{cq}} \gg \dfrac{\lambda_0(L_y - L)}{a}. \end{cases}$$

As a result, the SNR defined by (6.1) has the form

$$\mathrm{SNR}_{\mathrm{CC}} \approx \begin{cases} \dfrac{\sigma_{\mathrm{ref}} X_{\mathrm{cq}}^2}{\lambda_0^3 (L_y - L)^2} \dfrac{N_{\mathrm{s}}}{I_{\mathrm{s}}^{1/2}} \Big(\dfrac{B}{\omega_c}\Big)^{1/2} \dfrac{a^2}{\Delta X_{\mathrm{q}}^2} & \text{if } X_{\mathrm{cq}} \ll \Delta X_{\mathrm{q}}, \\[4mm] \dfrac{\sigma_{\mathrm{ref}} X_{\mathrm{cq}}^2}{\lambda_0^3 (L_y - L)^2} \dfrac{N_{\mathrm{s}}}{I_{\mathrm{s}}^{1/2}} \Big(\dfrac{B}{\omega_c}\Big)^{1/2} \dfrac{a^2}{X_{\mathrm{cq}}^2} & \text{if } X_{\mathrm{cq}} \gg \Delta X_{\mathrm{q}}. \end{cases}$$

Let us consider the quantity I_{s} defined by (6.2). If $X_{\mathrm{cs}} \ll \Delta X_{\mathrm{s}}$, then only the diagonal terms $s = s'$ survive in the double sum:

$$I_{\mathrm{s}} = \sum_{s,s'=1}^{N_{\mathrm{s}}} \exp\Big(-\frac{2|\boldsymbol{x}_s - \boldsymbol{x}_{s'}|^2}{X_{\mathrm{cs}}^2}\Big) \overset{X_{\mathrm{cs}} \ll \Delta X_{\mathrm{s}}}{=} \sum_{s=1}^{N_{\mathrm{s}}} \exp(0) = N_{\mathrm{s}}.$$

If $X_{\mathrm{cs}} \gg \Delta X_{\mathrm{s}}$, then we can apply the continuum approximation:

$$I_{\mathrm{s}} = \sum_{s,s'=1}^{N_{\mathrm{s}}} \exp\Big(-\frac{2|\boldsymbol{x}_s - \boldsymbol{x}_{s'}|^2}{X_{\mathrm{cs}}^2}\Big) \overset{X_{\mathrm{cs}} \gg \Delta X_{\mathrm{s}}}{=} \frac{1}{\Delta X_{\mathrm{s}}^2} \sum_{s=1}^{N_{\mathrm{s}}} \int_{[-b/2, b/2]^2} \exp\Big(-\frac{2|\boldsymbol{x}_s - \boldsymbol{x}|^2}{X_{\mathrm{cs}}^2}\Big) d\boldsymbol{x}.$$

Since we also have $b \gg X_{\mathrm{cs}}$, this can be simplified as

$$I_{\mathrm{s}} \overset{X_{\mathrm{cs}} \gg \Delta X_{\mathrm{s}}}{=} \frac{1}{\Delta X_{\mathrm{s}}^2} \sum_{s=1}^{N_{\mathrm{s}}} \int_{\mathbb{R}^2} \exp\Big(-\frac{2|\boldsymbol{x}_s - \boldsymbol{x}|^2}{X_{\mathrm{cs}}^2}\Big) d\boldsymbol{x} = \frac{N_{\mathrm{s}}}{\Delta X_{\mathrm{s}}^2} \frac{\pi X_{\mathrm{cs}}^2}{2},$$

so that we finally find

$$I_{\mathrm{s}} = \begin{cases} N_{\mathrm{s}} & \text{if } X_{\mathrm{cs}} \ll \Delta X_{\mathrm{s}}, \\ \dfrac{\pi N_{\mathrm{s}} X_{\mathrm{cs}}^2}{2\Delta X_{\mathrm{s}}^2} & \text{if } X_{\mathrm{cs}} \gg \Delta X_{\mathrm{s}}. \end{cases}$$

This gives

$$\frac{N_{\mathrm{s}}}{I_{\mathrm{s}}^{1/2}} \approx \begin{cases} \dfrac{b}{\Delta X_{\mathrm{s}}} & \text{if } X_{\mathrm{cs}} \ll \Delta X_{\mathrm{s}}, \\ \dfrac{b}{X_{\mathrm{cs}}} & \text{if } X_{\mathrm{cs}} \gg \Delta X_{\mathrm{s}}, \end{cases}$$

which completes the proof of the proposition.   ■

REFERENCES

[1] A. BAKULIN AND R. CALVERT, *The virtual source method: Theory and case study*, Geophysics, 71 (2006), pp. SI139–SI150.

[2] B. BIONDI, 3*D Seismic Imaging*, Society of Exploration Geophysics, Tulsa, 2006.

[3] N. BLEISTEIN, J. K. COHEN, AND J. W. STOCKWELL, *Mathematics of Multidimensional Seismic Imaging, Migration, and Inversion*, Springer, New York, 2001.

[4] L. BORCEA, J. GARNIER, G. PAPANICOLAOU, AND C. TSOGKA, *Enhanced statistical stability in coherent interferometric imaging*, Inverse Problems, 27 (2011), 085004.

[5] L. BORCEA, G. PAPANICOLAOU, AND C. TSOGKA, *Interferometric array imaging in clutter*, Inverse Problems, 21 (2005), pp. 1419–1460.

[6] L. BORCEA, G. PAPANICOLAOU, AND C. TSOGKA, *Adaptive interferometric imaging in clutter and optimal illumination*, Inverse Problems, 22 (2006), pp. 1405–1436.

[7] L. BORCEA, G. PAPANICOLAOU, AND C. TSOGKA, *Asymptotics for the space-time Wigner transform with applications to imaging*, in Stochastic Differential Equations: Theory and Applications, P. H. Baxendale and S. V. Lototsky, eds., Interdiscip. Math. Sci. 2, World Scientific, Hackensack, NJ, 2007, pp. 91–112.

[8] M. BORN AND E. WOLF, *Principles of Optics*, Cambridge University Press, Cambridge, UK, 1999.

[9] B. CLERCKX AND C. OESTGES, *MIMO Wireless Networks: Channels, Techniques and Standards for Multi-Antenna, Multi-User, and Multi-Cell Systems*, Academic Press, Oxford, UK, 2013.

[10] W. ELMORE AND M. HEALD, *Physics of Waves*, Dover, New York, 1969.

[11] A. FANNJIANG, *Information transfer in disordered media by broadband time-reversal: Stability, resolution and capacity*, Nonlinearity, 19 (2006), pp. 2425–2439.

[12] A. FANNJIANG, *Introduction to propagation, time reversal and imaging in random media*, in Multi-Scale Phenomena in Complex Fluids. Papers from the Summer School on Analysis and Numerics in Modern Sciences held at Fudan University, Shanghai, 2004 and 2006, Ser. Contemp. Appl. Math. CAM, 12, T. Y. Hou, C. Liu, and J. G. Liu, eds., World Scientific, Singapore, Higher Education Press, Beijing, 2009, pp. 111–174.

[13] J.-P. FOUQUE, J. GARNIER, G. PAPANICOLAOU, AND K. SØLNA, *Wave Propagation and Time Reversal in Randomly Layered Media*, Springer, New York, 2007.

[14] J.-P. FOUQUE, G. PAPANICOLAOU, AND Y. SAMUELIDES, *Forward and Markov approximation: The strong-intensity-fluctuations regime revisited*, Waves Random Media, 8 (1998), pp. 303–314.

[15] J. GARNIER, *Imaging in randomly layered media by cross-correlating noisy signals*, Multiscale Model. Simul., 4 (2005), pp. 610–640.

[16] J. GARNIER AND G. PAPANICOLAOU, *Passive sensor imaging using cross correlations of noisy signals in a scattering medium*, SIAM J. Imaging Sci., 2 (2009), pp. 396–437.

[17] J. GARNIER AND G. PAPANICOLAOU, *Resolution analysis for imaging with noise*, Inverse Problems, 26 (2010), 074001.

[18] J. GARNIER AND G. PAPANICOLAOU, *Correlation based virtual source imaging in strongly scattering media*, Inverse Problems, 28 (2012), 075002.

[19] J. GARNIER AND G. PAPANICOLAOU, *Role of scattering in virtual source array imaging*, SIAM J. Imaging Sci., 7 (2014), pp. 1210–1236.

[20] J. GARNIER AND K. SØLNA, *Coupled paraxial wave equations in random media in the white-noise regime*, Ann. Appl. Probab., 19 (2009), pp. 318–346.

[21] P. A. MARTIN, *Multiple Scattering. Interaction of Time-Harmonic Waves with N Obstacles*, Cambridge University Press, Cambridge, UK, 2006.

[22] A. ISHIMARU, *Wave Propagation and Scattering in Random Media. Vol.* II, Academic Press, New York, 1978.

[23] A. PAULRAJ, R. NABAR, AND D. GORE, *Introduction to Space-Time Wireless Communications*, Cambridge University Press, Cambridge, UK, 2003.

[24] M. C. W. VAN ROSSUM AND TH. M. NIEUWENHUIZEN, *Multiple scattering of classical waves: Microscopy, mesoscopy, and diffusion*, Rev. Mod. Phys., 71 (1999), pp. 313–371.

[25] G. T. SCHUSTER, *Seismic Interferometry*, Cambridge University Press, Cambridge, UK, 2009.

[26] V. I. TATARSKII AND V. U. ZAVOROTNY, *Strong fluctuations in light propagation in a randomly inhomogeneous medium*, Progress in Optics, 18 (1980), pp. 204–256.

[27] K. WAPENAAR, E. SLOB, R. SNIEDER, AND A. CURTIS, *Tutorial on seismic interferometry: Part 2—Underlying theory and new advances*, Geophysics, 75 (2010), pp. 75A211–75A227.